Late Cretaceous changes in oceanic currents and sediment sources in the eastern Tethys: insights from Nd isotopes and clay mineralogy

Elise Chenot, Emmanuelle Pucéat, Nicolas Freslon, Jean-François Deconinck, Mohammad Javad Razmjooei, Nicolas Thibault

Late Cretaceous changes in oceanic currents and sediment sources in the eastern Tethys: insights from Nd isotopes and clay mineralogy

Chenot Elise [a,b], Pucéat Emmanuelle [b], Freslon Nicolas [b], Deconinck Jean-François [b], Razmjooei Mohammad Javad [c,d], Thibault Nicolas [d]

Affiliations

[a] Institut Polytechnique Lasalle Beauvais, 19 Rue Pierre Waguet, BP 30313, F-60026 Beauvais, France

[b] Biogéosciences, UMR 6282, 6 boulevard Gabriel, Université Bourgogne Franche-Comté, F-21000 Dijon, France

[c] Department of Geology, Faculty of Earth Science, Shahid Beheshti University, Tehran, Iran

[d] IGN, Univ. of Copenhagen, Øster Voldgade 10, DK-1350 Copenhagen, Denmark

Corresponding authors: present address elise.chenot@unilasalle.fr & permanent address chenotelise@gmail.com

Co-authors: nicolas.freslon@u-bourgogne.fr; emmanuelle.puceat@u-bourgogne.fr; jean-francois.deconinck@u-bourgogne.fr; mj.razmjooei@gmail.com; nt@ign.ku.dk

Abstract

The Late Cretaceous is marked by geodynamical changes including Africa-Eurasia convergence that resulted in the narrowing of the Tethys Ocean and in ophiolite obduction along the southern margin of the various continental blocks in eastern Tethys. Geochemical and mineralogical analyses were performed on the Shahneshin section (Zagros Basin - eastern

Tethys), to explore the consequences of this evolution on oceanic circulation, and to estimate the role of ophiolite weathering that can impact climate through atmospheric CO_2 drawdown. [Ni] and [Cr] sharply increase in the uppermost Campanian – Maastrichtian interval and are not coeval with an increase in the Nd isotope composition (ε_{Nd}) of the detrital fraction of the sediments. This is interpreted as reflecting weathering of the mantellic, ultramafic part of the ophiolite sequence at that time, implying that ophiolites were exposed on the continents as soon as the Coniacian in the vicinity of the Zagros Basin. Hence their weathering could have contributed to the Late Cretaceous climatic cooling. Clay mineralogy reveals an alternation of kaolinite-rich humid periods (Coniacian/Santonian and late early Campanian to latest Campanian) and kaolinite-depleted arid periods (early Campanian and the latest Campanian to late Maastrichtian). The $\varepsilon_{Nd(t)}$ of bathyal waters (carbonate leached fraction) appears quite radiogenic, in the range of -3.4 to -5.2 ε-units, about 2 to 4 ε-units higher than the detrital fraction. Changes in the $\varepsilon_{Nd(t)}$ of detrital material delivered to the Zagros Basin appear to control the $\varepsilon_{Nd(t)}$ of the local bottom waters from the Coniacian to the middle Campanian. By contrast, decoupling of detrital $\varepsilon_{Nd(t)}$ from that of the local bottom waters from the middle Campanian to the Maastrichtian points to increasing fluxes of westward flowing Pacific radiogenic water masses into the eastern Tethys at that time. These results support an intensification of the Tethyan Circumglobal Current, likely related to the narrowing of the Tethyan seaway.

Keywords

Ocean circulation, Late Cretaceous, continental weathering, climate, Shahneshin section, Iran

1. Introduction

The Late Cretaceous was characterized by a long-term global cooling (Huber et al., 1995, 2002, 2018; Pucéat et al., 2003; Friedrich et al. 2012; Linnert et al., 2014) which has been linked to a decrease in atmospheric pCO_2 (Royer et al., 2012; Franks et al., 2014; Wang et al., 2014; Mills et al., 2019). During the last decades, many studies have investigated the processes involved in this atmospheric CO_2 evolution. A reduction in CO_2 mantle degassing, linked to a reduction in seafloor production rates and continental arc magmatism, has been repeatedly invoked to explain a decrease in pCO_2 during the Late Cretaceous (Cogné and Humler, 2006; Van der Meer et al., 2014; McKenzie et al., 2016). Enhanced CO_2 drawdown by continental weathering has also been suggested as a driver of this climate evolution (Jagoutz et al., 2016; Chenot et al., 2018), with a potentially important role of ophiolite obduction and weathering onto the southern Tethyan margin recently pointed out by Jagoutz et al. (2016). Whilst some constraints have been brought on the timing of the initiation of ophiolite obduction, notably using radiometric geochemical dating (Delaloye and Desmons, 1980; Lanphere and Pamić, 1983; Shahidi and Nazari, 1997; Tilton et al., 1981; Babaie et al., 2006; Shafaii Moghadam and Stern, 2011; Agard et al., 2011; Ao et al., 2016), information is still largely lacking on the timing of effective subaerial exposure of ophiolitic rocks to weathering processes, that can only be inferred from biostratigraphy of the overlying sediments (Shafaii Moghadam and Stern, 2015). This lack of information impedes our knowledge of the links between climate and obduction during the Late Cretaceous.

The ophiolite obduction that affected a large part of the southern Tethyan margin has been related to the dynamics of Africa-Eurasia convergence (Guiraud and Bosworth, 1997; Şengör and Stock, 2014; Jolivet et al., 2016). This convergence also resulted in a narrowing of the Tethys Ocean, with potential implications on oceanic circulation, a major component of the climate system. A major reorganization in the global oceanic circulation has been depicted

76 during the Late Cretaceous, evidenced during the Campanian by a decrease of 2 ε-units of the
77 Nd isotope composition of bottom waters, a tracer of modern and ancient ocean circulation, in
78 the Atlantic and Indian oceans (Robinson et al., 2010; Macleod et al., 2011; Murphy and
79 Thomas, 2012, 2013; Robinson and Vance, 2012; Voigt et al., 2013; Moiroud et al., 2016).
80 This 2 ε-units decrease could have marked the onset or intensification of deep-water
81 formation in the southern Atlantic (Robinson et al., 2010; Robinson and Vance, 2012;
82 Murphy and Thomas, 2012, 2013; Voigt et al., 2013) or in the northern Atlantic (Macleod et
83 al., 2011). The progressive narrowing of the Tethys during the Late Cretaceous, related to the
84 northward motion of Africa, may have played a role in this reorganization of the oceanic
85 circulation. The Tethys Ocean linked the proto-Indian and Atlantic oceans during the
86 Cretaceous, and formed, along with the open Caribbean seaway linking the Atlantic and
87 Pacific Oceans, a low-latitude seaway where seawater could flow unimpeded throughout the
88 globe. A large circum global current, called the Tethyan Circumglobal Current (TCC), is
89 thought to have flowed westward throughout this seaway (Föllmi et al., 1992; Pucéat et al.,
90 2005; Soudry et al., 2006). Like the modern Antarctic Circum global Current that flows
91 unimpeded around Antarctica, the TCC could have played a major role in the global oceanic
92 circulation, impacting the density balance between oceanic water masses through the transport
93 of salty waters. The development of intensive upwelling systems along the southern Tethyan
94 margin during the Campanian and Maastrichtian, which is marked by large phosphorite
95 deposits and high productivity of floro-faunal assemblages (*e.g.* Notholt, 1985; Almogi-Labin
96 et al., 1993; Eshet and Almogi-Labin, 1996; Ashckenazi-Polivoda et al., 2011), points to
97 potentially important modifications in the intensity of the TCC at that time.

98 In this context, we aim in this study at exploring the potential changes in the TCC
99 during the narrowing of the Tethys Ocean in the Late Cretaceous. We present a new dataset of
100 the $\varepsilon_{Nd(t)}$ of seawater inferred from the acetic acid-leached fraction of sediments collected

101 along the Shahneshin section (Zagros Basin, Iran), following recent development for the
102 acquisition of a seawater signal from different sediment fractions (Wilson et al., 2013). The
103 Shahneshin outcrop is located in the eastern part of the Tethys, close to the eastern entrance
104 into the Tethyan seaway. The $\varepsilon_{Nd(t)}$ of seawater at this site has thus the potential to track
105 changes in the TCC intensity. The evolution of clay mineral assemblages, of the $\varepsilon_{Nd(t)}$ of the
106 insoluble residual fraction of the sediment, and elemental (Ni and Cr) concentrations of the
107 sediments are also determined, to discuss the possible impact of changes in the source of
108 material eroded from the nearby continent on local seawater $\varepsilon_{Nd(t)}$ and to discuss the potential
109 links between weathering and erosion processes in this region, ophiolite obduction, and
110 climate.
111
112 2. Geodynamical framework and palaeogeography
113
114 The Middle East region presents highly deformed sedimentary structures in the
115 orogenic areas (Zagros, Caucasus) and metamorphic rocks around the obducted areas
116 (Cyprus, Northern Turkey, Syria, south of Iran, Oman; Fig. 1). This modern geological
117 framework is linked to the anticlockwise movement of Africa initiated during the Cretaceous,
118 which ultimately led to the closure of the Tethyan Realm and to the subduction of the Neo-
119 Tethys Ocean beneath central Iran (Bosworth et al., 1999; Jolivet et al., 2016). In the eastern
120 part of the Tethys, this tectonic event is expressed by a 5,000 km-long region of relief
121 developed across the north of Africa and the Middle East, called the Ayyubid orogeny. It is
122 associated to the establishment of a widespread ophiolitic belt along the Afro-Arabian passive
123 continental margin during the Turonian to Campanian interval (Agard et al., 2005; Homke et
124 al., 2009; Shafaii Moghadam and Stern, 2011; Şengör and Stock, 2014; Jolivet et al., 2016;
125 Fig. 1). This compressional tectonic regime has induced the development of highly subsiding

126 basins and inversion reliefs (*e.g.* Zagros folded zone; Koop and Stoneley, 1982; Agard et al.,
127 2005; Homke et al., 2009; Şengör and Stock, 2014). Weathering of newly created nearby
128 continental masses most likely provided detrital particles transported and deposited into
129 adjacent highly subsiding basins (Saura et al., 2011).
130
131 2.1. Zagros basin and the "Gurpi" Formation
132
133 The Zagros folded zone encompasses south-eastern Turkey, northern Syria, northern
134 Iraq and western to southern parts of Iran (Alavi, 1980, 1994; Berberian and King, 1981;
135 Dercourt et al., 1986; Fig. 1a). In the west and southwestern parts of Iran, this NW-SE folded
136 structure is composed of four main mountains provinces called Lurestan, Khuzestan, Internals
137 Fars and Coastal Fars at about 26 to 35° N (Agard et al., 2005; Fig. 1a). Palaeogeographical
138 reconstructions suggest a palaeolatitude of 5 to 10° N for the Zagros Basin during the
139 Campanian and Maastrichtian (Philip and Floquet, 2000; Barrier and Vrielynck, 2007; Fig.
140 1b-c). This basin is located within the equatorial Tethyan corridor, bordered to the south by
141 the Arabian Shield, and to the north by an active subduction zone with ophiolitic nappes,
142 possibly above sea-level during the early Campanian and immersed during the late
143 Maastrichtian (Barrier and Vrielynck, 2007; Fig 1b-c). The ages of the sediments overlying
144 the mantellic and crustal rocks, that provide an age range of the sub-aerial exposure of the
145 Iranian Zagros ophiolites, are Triassic to Cretaceous for Kermanshah ophiolites (Lurestan;
146 Saccani et al., 2013; Whitechurch et al., 2013; Shafaii Moghadam and Stern, 2015),
147 Cenomanian-Turonian to early Santonian for Neyriz ophiolites (Babaei et al., 2006; Shafaii
148 Moghadam and Stern, 2011), undifferentiated Late Cretaceous for Haji Abad ophiolites
149 (Ghasemi et al., 2002), and late Turonian to Maastrichtian for Baft ophiolites (Fars Provinces;
150 Shafaii Moghadam and Stern, 2011; Shafaii Moghadam et al., 2013).

The Late Cretaceous sedimentation of the Zagros Basin (Coniacian to Maastrichtian) consists of organic matter-rich marls and limestones which compose the Gurpi Formation (Fm. - average of 3% of total organic carbon; Ala et al., 1980). This formation is largely outcropping in the four main Zagros mountain provinces (Fig. 1c). Several hiatuses are recorded in the Gurpi Fm., which have been related to maximum flooding surfaces and/or tectonic events (Razmjooei et al., 2014, 2018, 2020a; Zarei and Ghasemi-Nejad, 2015). The dinoflagellate diversity associated to the microfossil assemblages (planktonic and benthic foraminifera) highlight the existence of lateral variability of facies in the Gurpi Fm. The Fars province displays external ramp environments whereas the Lurestan and the Khuzestan Province record shallower environments characterized by two bioturbated and fossiliferous limestones units called the "*Lopha* limestone member" (late Campanian, *Globotruncana aegyptica* biozone) and the "Emam Hassan member" (late Campanian to early Maastrichtian, *Gansserina gansseri* biozone; Zarei and Ghasemi-Nejad, 2015). This facies lateral variability recorded in the Gurpi Fm., associated to regional gaps, has been linked to compressive tectonic movements generating different subsidence rates between provinces.

2.2. Shahneshin section

The investigated Late Cretaceous deposits of the Gurpi Fm. are located in the central part of the Zagros folded zone, west of the Fars province, to the north east of Kazerun city and the north west of the Shahneshin anticline (N 29° 44' 47" and E 51° 46' 31" for the base and 29° 44' 40.69" and E 51° 46' 26.87" for the top of the studied interval at Shahneshin). At Shahneshin, the sediments are composed of dark grey marls and light yellow argillaceous limestones alternations (Fig. 2). The marls and marly limestones of the Gurpi Fm. have been

deposited in a deep sedimentary basin (Motiei, 1993). Hemmati-Nasab et al. (2008) and Darabi et al. (2018) respectively suggest rough estimations of 800 to 1200m and 450 to 600m paleo-water depth for the Gurpi Fm. in Lurestan area. Occurrence of a very high abundance of benthic foraminifers in the upper Campanian of Shahneshin suggests a much shallower condition at this time, which could be due to a tectonically-induced regression caused by a phase of uplift (Razmjooei et al., 2018, 2020a).

The age-model relies on the integrated stratigraphic study of the Shahneshin section by Razmjooei et al. (2018; Fig. 3). Slight modifications were however proposed later on by Razmjooei et al. (2020a) for the basal part of the section based on carbon-isotope stratigraphy. In particular, the authors applied in Razmjooei et al. (2018) the biostratigraphic concept of the Coniacian/Santonian boundary based on the first occurrence of nannofossil *L. cayeuxii* at 20m. In Razmjooei et al. (2020a), the authors argued for the level of the Kingsdown carbon isotope event at 40 m being the best possible marker for the Coniacian/Santonian boundary, assuming some degree of plankton diachronism. This interpretation is kept here. Subsequently, the age-model applied here considers eight anchor points (Table 1; Suppl. Fig. 1). Out of these, the base Maastrichtian at 72.15 Ma is at the level identified in Razmjooei et al. (2018) but also accounts immediately for a ca. 2 Myr hiatus truncating the late Campanian (Suppl. Fig. 1). The FO of *G. aegyptiaca*, LO of *M. furcatus* and LO of *D. asymetrica* are given as in Razmjooei et al. (2018) age-model, the Kingsdown event is considered as the level of the Coniacian/Santonian boundary at 86.49 Ma and the basal 40 m of the section are considered to follow a similar sedimentation rate of 2.36cm/kyr as the interval above between 40 and 94m, thus giving an age of 88.19 Ma for the base of the section. This well-constrained age model reveals important changes in the sedimentation rate along the section, from approximately 2.4cm/kyr in the upper Coniacian to Santonian, around 0.6cm/kyr in the lowermost Campanian, to 2.5cm/kyr in the remaining of the Campanian. A significant gap,

possibly of up to 2 Ma, has been suggested to occur also in the uppermost Campanian to lowermost Maastrichtian, at 280 to 290m (Razmjooei et al., 2018; Suppl. Fig. 1).

3. Material and methods

3.1. Clay mineralogy

For detailed fieldwork and sampling strategy, we refer here to Razmjooei et al. (2018). Our sampling resolution for clay mineralogy varies between 1m and 5m. Mineralogical analyses have been performed at the Biogéosciences Laboratory (University of Bourgogne-Franche Comté, Dijon, France). Clay mineral assemblages of 120 samples have been identified by X-ray diffraction (XRD) on oriented mounts of non-calcareous clay-sized particles (<2 µm). The procedure described by Moore and Reynolds (1997) has been used to prepare the samples. Diffractograms have been obtained using a Bruker D4 Endeavor diffractometer with CuK_{α} radiations with LynxEye detector and Ni filter, under 40-kV voltage and 25-mA intensity. Three preparations have been analysed, after air-drying, after ethylene-glycol solvation and after heating at 490°C for 2h (Fig. 4). The goniometer scanned from 2.5° to 28.5° for each run. Clay minerals have been identified by the position of their main diffraction peaks on the three XRD runs, while semi-quantitative estimates have been produced in relation to their area (Moore and Reynolds, 1997). Areas have been determined on diffractograms of glycolated runs with MacDiff 4.2.5. Software (Petschick, 2000). Beyond the evaluation of the absolute proportions of the clay minerals, the aim was to identify their relative fluctuations along the section.

3.2. Rare earth elements concentrations (REE) and neodymium (Nd) isotope analyses

226

227 3.2.1. Sample preparation: carbonate and insoluble fraction extraction

228

229 Eighteen sedimentary bulk rock samples from the Shahneshin section were finely
230 crushed using an agate mortar and pestle. Aliquots of about 1.5g of powdered sediments were
231 leached with 20ml of acetic acid solution (2%) during 30 minutes in Teflon vial (Savillex®).
232 This short leaching time using quite diluted acetic acid aims to dissolve part of the carbonates
233 while limiting extraction of Fe-Mn oxides and/or reactive minerals (Wilson et al., 2013). The
234 solution was filtered (0.45µm, PTFE), evaporated to dryness and then re-dissolved with 4M
235 hydrochloric acid (HCl).

236 Another aliquot of about 2g of each powdered sediment sample went through the 3-
237 step leaching procedure derived from Bayon et al. (2002). Carbonate was removed using 20ml
238 acetic acid (10%, AA) that reacted overnight (about 18h), then Fe-Mn oxides were removed
239 using a 20ml reductive solution (25% acetic acid + 1M Hydroxylammonium Hydrochloride,
240 AA+HH) during 6 hours, and organic matter was removed using a 5% hydrogen peroxide
241 solution (H_2O_2, %wt/v) that reacted overnight (Tessier et al., 1979; Bayon et al., 2002). About
242 100mg of the residue was then digested using alkaline fusion following Bayon et al. (2009)
243 and the precipitated Fe-oxy-hydroxides dissolved in 4M hydrochloric acid (HCl).

244

245 3.2.2. Determination of the REE concentrations

246

247 Trace elements abundances in the carbonate leachates and the residue were determined
248 using an aliquot of the final mother solutions diluted in 10 ml HNO_3 2% (v/v). The REE
249 concentrations were measured with a quadrupole inductively coupled plasma mass
250 spectrometer (Thermo X-Series II) at the “Pôle Spectrométrie Océan” (IUEM Brest, France),

using the Tm addition method (Barrat et al., 1996; Bayon et al., 2009). The REE were measured in low resolution mode, and polyatomic oxide and hydroxide interferences were corrected using oxide formation rates determined by analyzing solutions of ultrapure water, Ba + Ce, Pr + Nd and Sm + Eu + Gd + Tb at the beginning of the measurement cycle. The uncertainty on all measurements was better than 5% for REE. The accuracy of the method was monitored by repeated analyses of two certified reference materials from USGS (BHVO-2 and BCR-2); deviation from the certified values (Jochum et al., 2016) was better than 5% for all replicates.

3.2.3. Determination of the Nd isotopic composition

The REE were isolated using common ion exchange chromatography, including a first ion exchange resin to isolate the lanthanides (AG-50W-X8, Bio-Rad) and a second one (Ln resin, Eichrom) to isolate Nd (Bayon et al., 2012). The Nd isotopic compositions of the residues were carried on a Multi-Collector MC-ICP-MS (Neptune, Thermo Scientific) at the "Pôle Spectrométrie Océan" (IFREMER Brest, France) with instrumental bias corrected by a sample-standard bracketing method, using *JNdi-1* (Tanaka et al., 2000). The carbonate leachate Nd isotope compositions were determined at the LGLTPE laboratory in Lyon (Ecole Normale Supérieure de Lyon, France) on a Thermo Scientific Neptune and a Nu Plasma 1700 MC-ICP-MS, using the *Rennes in-house* Nd standard (Chauvel and Blichert-Toft, 2001) as internal standard. All $^{143}Nd/^{144}Nd$ ratios were normalized to a value of 0.7219 for $^{146}Nd/^{144}Nd$ (Table 2). The 2s external reproducibility of our measurements was estimated using repeated analyses of the *JNdi-1* (0.512115 ± 0.000016; average ± 2s) and the *Rennes in-house* Nd standard (0.511961 ± 0.000009). The overall reproducibility of the chemistry is estimated by repeated analyses of the BHVO-2 certified reference material. During the course of the study,

276 the measured $^{143}Nd/^{144}Nd$ ratios of BHVO-2 were 0.512987 ± 0.000005 (average ± 2s; n=5)
277 and 0.512988 ± 0.000007 (n=12) by using the *JNdi-1* and the *Rennes in-house* Nd as internal
278 standard, respectively. Those values agree well with the reference values for MC-ICP-MS and
279 TIMS measurements (respectively 0.512990 ± 0.000010 and 0.512984 ± 0.000011; Weis et
280 al., 2006).
281
282 3.2.4. Post-sedimentation decay correction
283
284 The present-day Nd isotopic ratios measured in the samples were corrected for the
285 radioactive decay of ^{147}Sm to ^{143}Nd using the measured Sm and Nd concentrations determined
286 for each sample ($^{147}Sm/^{144}Nd$ = 0.6049 x [Sm]/[Nd]) and a radioactive decay constant λ =
287 $6.539.10^{-12}$ yr^{-1} for the Sm-Nd system (Begemann et al., 2001). The absolute ages of the
288 Shahneshin samples were calculated using the age model described in the Part 2.2 above and
289 in Table 1. The age-corrected isotopic ratios are expressed using the standard $\varepsilon_{Nd(t)}$ notation,
290 which corresponds to the relative deviation in part per thousand from the Chondritic Uniform
291 Reservoir (CHUR) values at the deposition age, using the present-day $^{143}Nd/^{144}Nd$ ratio of
292 0.512630 and $^{147}Sm/^{144}Nd$ ratio of 0.1960 for the CHUR (Bouvier et al., 2008). The analytical
293 uncertainties expressed under the $\varepsilon_{Nd(t)}$ notation, estimated by propagating external errors
294 introduced by the $^{143}Nd/^{144}Nd$ (±0.000016 or ±0.000009, ±2σ) and $^{147}Sm/^{144}Nd$ (±0.004, ±2σ),
295 are ±0.35 for the insoluble fractions and ±0.21 for the carbonate leachates (Table 2).
296
297 3.3. Determination of major and trace element concentrations
298
299 Twenty-two bulk sediment samples were additionally analysed for their major (Al)
300 and trace-element (Ni, Cr) concentrations at the Service d'Analyse des Roches et des

Minéraux of the Centre National de la Recherche Scientifique (SARM, Vandœuvre-lès-Nancy, France). Complete analytical procedure developed at the SARM is detailed in Carignan et al. (2001). About 300mg of powdered rock samples are fused in Pt crucibles with ultrapure $LiBO_2$ at 980°C in an oven for 60 min, and after cooling the fusion glass is dissolved in a HNO_3 (1 mol/l) - H_2O_2 (0.5% v/v) – glycerol (10% v/v) mixture. The samples were analysed on an ICP-OES (Thermo Fisher iCap 6500) and an ICP-MS (Thermo Fisher iCapQ), respectively, at the Service d'Analyse des Roches et des Minéraux of the Centre National de la Recherche Scientifique (SARM, Vandœuvre-lès-Nancy, France). Uncertainties in measurements, based on analyses of international reference standards (BR, AN-G, UB-N, DR-N, and GH; Govindaraju, 1995) and replicates are lower than 15% for Al_2O_3, and 5% for Ni and Cr (Table 2).

In order to discriminate changes in nickel (Ni) and chromium (Cr) concentration of the detrital material from variations in detrital supply, trace element concentrations have been normalized to Al, as aluminum is considered as a robust tracer of detrital input, and are expressed as element/Al (X/Al) ratios in this study (Fig. 3).

4. Results

4.1. Clay mineralogical assemblages

Clay mineral assemblages of the Shahneshin section are composed of illite-smectite mixed-layers (I-S R1), illite, kaolinite, chlorite, and likely a mixture of random mixed-layers including chlorite-smectite (C-S) chlorite-vermiculite (C-V) and finally vermiculite whose presence is suggested by the relatively narrow reflection at 14 Å which is not modified after saturation with ethylene-glycol and which decreases sharply after heating (Fig. 4). From the

base to 260m, I-S R1 dominates the clay fraction (35 to 40%) and decreases to 20% from 260m to the top of the section. Four mineralogical intervals are identified:

- Interval 1 (Coniacian-Santonian):

From the base to 80m, illite (20 to 30%) is associated to I-S R1 and abundant kaolinite reaching 50% at the base of the section and showing a mixture of C-S and C-V (and vermiculite?; 10%) decreasing proportions upward.

- Interval 2 (lowermost Campanian *pars*):

From 80 to 130m, the interval is characterized by increasing proportions of illite and I-S R1 and by the absence of kaolinite. Chlorite is occasionally abundant (up to 30%).

- Interval 3 (lower Campanian *pars* to upper Campanian):

From 130m to 250m, illite and I-S R1 decrease up section to 15% and less than 40% respectively. The proportions of chlorite never exceed 10%, while the proportions of kaolinite progressively increase up to 40% from the base to the top of the interval.

- Interval 4 (uppermost Campanian and Maastrichtian):

From 250m to the top of the section, chlorite and illite increase again (respectively 35% and 20%). In the same interval, the mixture of C-S, C-V and vermiculite increases significantly around 30%.

4.2. REE concentrations and Nd isotopes

REE concentrations for the insoluble fractions and the acetic acid leachates are reported on Table 2 and are presented on Fig. 5 normalized to PAAS (Post Archean Australian Shale; Taylor and McLenann, 1985). The insoluble fractions all display quite similar REE patterns, characterized by depletion in Middle Rare Earth Element (MREE) and a very small or absent cerium (Ce) anomaly. By contrast, the acid acetic leachates of all

samples display a negative Ce anomaly and enrichment in middle and heavy REEs, with lower REEs concentrations compared to the insoluble fraction. The acetic acid leachates yield systematically more radiogenic Nd isotopic values than the corresponding insoluble fractions, of about 3 ε-units on average, but up to about 4 ε-units (Table 2; Fig. 3). The insoluble fraction $\varepsilon_{Nd(t)}$ ranges from -9.0 to -6.0 ε-units and shows a positive excursion encompassing an interval from the Coniacian to the uppermost Santonian, with $\varepsilon_{Nd(t)}$ reaching maximum values of about -6 ε-units during the Santonian. Insoluble fraction $\varepsilon_{Nd(t)}$ remains around -8 ε-units, within the exception of one sample (ShG E07) that yield a value of -6.8 ε-units, until the lower Campanian where $\varepsilon_{Nd(t)}$ values increase again by about 2 ε-units, from -8.1 to -6.2 ε-units in the uppermost lower Campanian. $\varepsilon_{Nd(t)}$ values then decrease by about 3 ε-units, down to -9 ε-units in the upper Maastrichtian at the top of the section. The acetic leachate $\varepsilon_{Nd(t)}$ displays a similar evolution than that of the insoluble fraction, with an offset of about 2-3 ε-units toward more radiogenic values, from the Coniacian to the uppermost Santonian. By contrast, acetic leachate $\varepsilon_{Nd(t)}$ values remain quite stable, around -4 ε-units, until the lower Maastrichtian and then decline slightly from the lower to the upper Maastrichtian down to values of about -4.5 ε-units.

4.3. Major and trace element concentrations

Analytical results for the twenty-two samples are shown in Table 3 and Fig. 3. The chemical data of trace elements show that the CaO, SiO_2 and Al_2O_3 contents ranges are 36-48 wt.%, 7–18 wt.% and 2–7 wt.% respectively, and the chemical data of trace elements show that Ni and Cr contents ranges are 21-83 ppm and 42-101 ppm range. Thus, the bulk rocks of the Shahneshin section are rich in CaO, SiO_2 and Al_2O_3, while depleted in Fe_2O_3, K_2O, TiO_2, and MgO. An important characteristic of these carbonates is the highest proportions of Ni and

Cr from 250m to the top of the section (upper Campanian to upper Maastrichtian), showed by markedly higher ratios of Ni/Al and Cr/Al above 250m (Fig. 3).

5. Discussion

5.1. Diagenesis of the clay minerals

To interpret clay mineral assemblages in terms of palaeoenvironments, we have to ensure that post depositional transformations including burial diagenesis did not modify significantly the clay minerals and that their initial sedimentary signal is preserved. In this relatively thick section from a highly tectonised area, thermal influences may be expected to have played a significant role on clay mineral assemblages. The influence of a thermal diagenesis is even more probable that the clay assemblages are devoid of I-S R0 comparable to smectites (Fig. 3). This absence is surprising because in the Tethyan Realm and even all over the globe, the Late Cretaceous is marked by a clay sedimentation largely dominated by smectites (Chamley, 1989; Chamley et al., 1990; Thiry and Jacquin, 1993; Deconinck and Chamley, 1995; Chenot et al., 2018). Moreover, there is an abundance of I-S R1 and a complex mixture of C-S and C-V mixed-layering which are respectively all intermediate phases of the transformation of smectites into illite and chlorite. However, from the top to the bottom of the section, the proportions of illite, chlorite and mixed-layers do not increase steadily, as would have been expected under a strong influence of burial diagenesis. The preservation of kaolinite, which is also sensitive to burial diagenesis, suggests that maximum burial temperature was not high enough (<150°C, Beaufort et al., 2015) to transform this mineral, whose fluctuations seem to correspond to a primary signal (Fig. 3).

To sum up, it is likely that the initial clay sedimentation included a significant

proportion of I-S R0 (smectite) but that these minerals under mild thermal influence turned into I-S R1, C-S and C-V mixed-layers. In addition, this is in agreement with the moderate to poor preservation of the nannofossils (Razmjooei et al., 2020b). However, the evolution of the relative proportions of illite, chlorite and kaolinite seem to be mainly a primary signal that can be interpreted in terms of palaeoenvironment and palaeoclimate.

5.2. Climatic control of the clay assemblages of the Shahneshin section

The most striking feature of the clay mineralogy of the Shahneshin section is the alternation of kaolinite-rich intervals with intervals devoid of kaolinite (Fig. 6). The formation of kaolinite in soils requires a high level of hydrolysis and consequently a significant humidity and runoff favoring water renewal. A high temperature accelerates the hydrolysis reactions but humidity is the key parameter to form kaolinite in weathering profiles, (Chamley, 1989; Ruffell et al., 2002). Currently, kaolinite is abundant in weathering profiles that developed mainly at low latitudes. Fluctuations in kaolinite proportion in clay assemblages, especially when they are linked to opposite trends in illite and chlorite that derive from weathering and erosion of the basement in more arid environments, is often interpreted in terms of changes in humidity/aridity (*eg.* Vanderaveroet et al., 1999; Adatte et al., 2002; Moiroud et al., 2012). Kaolinite can also be reworked from old non-metamorphosed rocks. In this case, it is generally accompanied by primary minerals (illite and chlorite), often abundant in ancient rocks that underwent significant diagenesis (Chenot et al., 2016). On the Shahneshin section, percentages of illite and chlorite do not show the same trends as kaolinite but rather display opposite trends. This suggests that kaolinite is most likely reworked from pedogenic blankets developed at the time of sedimentation, which points to the existence, at the time of kaolinite deposition, of a relatively warm and humid climate. Such climatic

conditions are supported by the occurrence of bauxites on emerged peri-Tethyan continental masses during the Late Cretaceous (Bárdossy and Dercourt, 1990), and by the compilation of lithological and paleontological indicators, including vegetation (Otto-Bliesner and Upchurch, 1997; Upchurch et al., 2015). By contrast, the intervals with little or no kaolinite, that present higher proportions of illite and chlorite in the clay mineral assemblages, would then point to a drier climate during these intervals. Interestingly, the locally drier climatic conditions recorded during the late Campanian to Maastrichtian at Shahneshin (mineralogical interval 4, Fig. 3) do not reflect the overall humid conditions (kaolinite up to 60-80%) recorded at other tethyan sites with paleolatitudes comprised between approximately 0 and 25°N (Tunisia, Li et al., 2000; Adatte et al., 2002; Egypt, Tantawy et al., 2001; Keller et al., 2002; Iran, Rostami et al., 2018; Italy; Chenot et al., 2018). This feature may be related to the specific paleogeography of the Zagros region, inducing different local climatic conditions in the Zagros studied area in this interval.

It is thus likely that an evolution in local climate could have contributed to the observed changes in clay mineral assemblages (Fig. 6). More humid conditions in intervals 1 (Coniacian to latest Santonian) and 3 (middle Campanian to earliest late Campanian) could have favoured kaolinite formation, while more arid environments in intervals 2 (early Campanian) and 4 (late Campanian to late Maastrichtian) rather favoured formation of illite and chlorite. Surface marine temperatures inferred from TEX86 values at a comparable latitude in Israel highlight a cooling of a few degrees from the Coniacian to the early Campanian, but remain relatively stable up to the end of early Maastrichtian and do not show any correspondence with the evolution of clay mineralogy on the remaining of the section (Fig. 6; Alsenz et al., 2013). Yet surface temperatures recorded in Israel (Adheret 1 borehole and PAMA Quarry) are likely affected by the development of a large upwelling system during the Campanian and Maastrichtian, depicted by the occurrence of large phosphorite deposits

451 and floro-faunal assemblages of high productivity (Nothold, 1985; Almogi-Labin et al., 1993;
452 Ashckenazi-Polivoda et al., 2011). At a global scale, climate fluctuations are identified within
453 the Campanian-Maastrichtian interval, with a warming episode evidenced in benthic
454 foraminifera $\delta^{18}O$, in TEX86, and in planktonic foraminifera during the mid-late Campanian
455 (Friedrich et al., 2012; Linnert et al., 2014; Falzoni et al., 2016: Fig. 6). These climate
456 fluctuations may have modified to some extent the hydrological cycle and changed the local
457 hydrolysing conditions in the vicinity of the Zagros Basin. Such changes in sea-surface
458 temperatures of the central part of the Zagros Basin are also suggested from calcareous
459 nannofossil assemblages (Razmjooei et al., 2020b).

460 Variations in detrital sources are also susceptible to drive changes in clay
461 mineralogical assemblages through time (Fig. 6). The main geodynamical evolution evident in
462 this area is the 5,000 km long obduction-driven orogeny that affected the southern Tethyan
463 margin from Lybia to Oman, linked to Africa-Eurasia convergence during the Late
464 Cretaceous (Agard et al., 2011; Şengör and Stock, 2014). On both sides of the intra-oceanic
465 subduction zone in the Zagros area, two ophiolitic belts were obducted, parallel to the south-
466 western part of Iran. These complete ophiolites sequences contain well-preserved mantellic
467 (harzburgite) and crustal (gabbro and basalt) rocks (Shafaii Moghadam and Stern, 2011).
468 Because of their mineralogical composition, oceanic crust rocks are very sensitive to chemical
469 weathering, and plagioclase feldspar (basalt and gabbro's major components) degradation
470 could provide the aluminum required to form kaolinite, incorporated in lateritic profiles
471 widespread at low latitudes (Schopka et al., 2011; Giorgis et al., 2014). Illite and chlorite are
472 primary minerals deriving from weathering and erosion of felsic, chlorite and mica-rich
473 metamorphic rocks from the basement.

474 However, if the evolution of clay assemblages along the Late Cretaceous Shahneshin
475 section was controlled by changes in the nature and provenance of the weathered and eroded

476 rocks as sediment sources, a co-variation of kaolinite proportions with Ni/Al and Cr/Al ratios
477 would be expected, that is not observed here (Fig. 6). Indeed, mafic and ultramafic rocks are
478 notably concentrated in Ni and Cr (Azizi et al., 2013; MacKay and Ansdell, 2013), and
479 detrital material eroded from such rocks and deposited nearby is expected to be enriched in Ni
480 and Cr compared to material derived from weathering of crystalline basement. On the
481 contrary, bulk rock Cr/Al and Ni/Al evolution along the section appears to be decoupled from
482 the evolution in kaolinite proportions. The Cr/Al and Ni/Al ratios both display a sharp
483 increase in the middle and late Campanian followed by a milder increase in the Maastrichtian,
484 while kaolinite proportions decrease to values close to zero at the end of the late Campanian
485 and remain close to zero afterwards, after the ca. 2Myr hiatus.

486 The evolution of Ni and Cr concentrations in the sediments do not support a change in
487 the source of the detrital material as the main driver of clay mineral assemblage evolution in
488 the studied section, between an ophiolite source generating kaolinite and a crystalline
489 basement source generating illite and chlorite. More likely, evolution of clay mineral
490 assemblages is controlled by changes in hydrolysing conditions in the studied area, with
491 kaolinite-rich intervals reflecting more humid conditions and illite and chlorite-rich intervals
492 reflecting drier conditions. The increase in Ni/Al and Cr/Al ratios from the middle Campanian
493 to the Maastrichtian may either mark the initiation of ophiolite weathering in this region, or of
494 the weathering of the ultramafic, mantellic part of the ophiolite sequence that is over 10 times
495 more enriched in Ni and Cr than the overlying basalt and gabbros (Azizi et al., 2013; Shafaii
496 Moghadam and Stern, 2015; Nouri et al., 2019; Monsef et al., 2018). Weathering of mafic and
497 ultramafic rocks can also provide the high magnesium content required to form chlorite and
498 vermiculitic clays at the expense of smectites.

499

500 5.3. Evolution of the insoluble fraction $\varepsilon_{Nd(t)}$: insights on ophiolite weathering in Iran?

Detrital particles derived from the weathering and erosion of the bedrock retain the initial Nd isotope signature of the source rock (Goldstein et al., 1984). The Nd isotope signature of the detrital fraction recovered from marine sediments has thus been widely used to track sediment provenance (*e.g.* Frank et al., 2002; Goldstein and Hemming, 2003; Revel et al., 2010; van der Lubbe et al., 2016). Mantellic material, characterized by high Sm/Nd ratios, yield high ε_{Nd} values reflecting a radiogenic composition, while ancient crustal material, characterized by lower Sm/Nd ratios, yield negative ε_{Nd} values reflecting an unradiogenic composition.

The insoluble fraction analyzed in this work represents the residue obtained after removal of carbonates, Fe-Mn oxides, and organic matter from bulk sediment samples using acetic acid, hydroxyl-ammonium hydrochloride, and hydrogen peroxide respectively (Fig. 6, *see the Material and Method part*). In distal oceanic sites, authigenic clays can in some case contribute significantly to the insoluble fraction of the sediments which in that case may partly integrate the Nd isotope composition of bottom seawater (Chamley and Bonnot-Courtois, 1981; Dubinin, 2004; Karpoff et al., 2007). At Shahneshin, the sediments have been deposited in a bathyal environment within an oceanic channel during the Late Cretaceous (Fig. 1), relatively close to the continent. This proximity to land masses is also highlighted by the quite high sedimentation rate recorded throughout the section (Razmjooei et al., 2018; Suppl. Fig. 1). Therefore, we think it unlikely for authigenic clays to represent a significant part of the insoluble fraction, and interpret the $\varepsilon_{Nd(t)}$ of this fraction as mostly reflecting the Nd isotope composition of local detrital inputs (Fig. 6). This view is supported by the REE pattern of the residue that is quite different from that of seawater characterized by a negative Ce anomaly, by depletion in light REE and enrichment in heavy REE (Fig. 5).

The decrease in $\varepsilon_{Nd(t)}$ of the detrital fraction during the sharp rise in Ni/Al and Cr/Al

ratios recorded in the middle Campanian to Maastrichtian interval argues against an initiation of ophiolite weathering at that time, that should rather be associated by a large increase in $\varepsilon_{Nd(t)}$ values. The Nd isotope data rather support weathering of the mantellic ultramafic material (mantellic rocks) underlying basalt and gabbro (volcanic and crustal rocks) of the ophiolite sequence as a driver for the observed increase in Ni/Al and Cr/Al ratios. Ultramafic peridotites are much more enriched in Ni and Cr (Azizi et al., 2013; Shafaii Moghadam et al., 2014; Monsef et al., 2018; Nouri et al., 2019) but are not expected to markedly increase the $\varepsilon_{Nd(t)}$ value of detrital material (Blusztajn et al., 1995), compared to that derived from the weathering of the overlying basalt and gabbros of the ophiolite sequence. If this interpretation is correct, our data then imply that ophiolite weathering was already initiated in the vicinity of the Zagros region during the Coniacian, at the base of the section, at least for the upper parts of the ophiolite sequences.

The decrease in Nd isotope values of the detrital fraction recorded from the middle Campanian to the Maastrichtian requires however the existence of an increasing input of an additional material with an unradiogenic composition (Fig. 6). The Nd isotope composition of the detrital fraction, in the range of -9 to -6 ε-units, actually appears quite unradiogenic all along the section considering the age and nature of the potentially exposed terranes in the vicinity of the Zagros Basin at that time, that are expected to deliver detrital material with a more radiogenic composition. The Nd isotope composition of obducted ophiolites both in the Outer and Inner Zagros Ophiolitic Belts is radiogenic, with $\varepsilon_{Nd(t)}$ values at 80 Ma in the range of +4.9 to +9.8 ε-units (Shafaii Moghadam et al., 2012; Azizi et al., 2013; Shafaii Moghadam et al., 2014). Granitoid bodies formed prior to the Late Cretaceous and outcropping at present in Iran also tend to present relatively radiogenic ε_{Nd} values (*e.g.* -3.5 to -2.9 ε-units calculated at 80 Ma for the Tuyeh-Darvar Granitoid, Naderi et al., 2018, Suppl. Table 1; or -4 to +1.2 ε-units at 80 Ma for the granitoid body of the Misho region in northwest Iran, although two

551 samples yield more unradiogenic values of -6.4 and -9.7 ε-units; Ahankoub et al., 2013, Fig.
552 7; Suppl. Table 1).

553 The relatively low ε_{Nd} values of the insoluble fraction, down to -9 ε-units, thus require
554 mixing with an additional, unradiogenic source, with inputs that could have varied along the
555 section. In a recent study, Nouri et al. (2019) has shown that some parts of the Harsin-Sahneh
556 serpentinized peridotites in the mantle sequence of the Zagros ophiolite complex, exposed
557 along the Zagros suture zone in western Iran, yield more unradiogenic values, down to -7.8 ε-
558 units at 80 Ma (Fig. 7; Suppl. Table 1). These low values have been interpreted by these
559 authors as reflecting interaction of peridotites with seawater during metasomatism in a supra-
560 subduction zone system. Alteration of serpentinized peridotites may have partly contributed to
561 the relatively low $\varepsilon_{Nd(t)}$ values observed in the insoluble fraction of Shahneshin. Other sources
562 of unradiogenic material, farther away from the studied area, are the Khida terrane within the
563 Arabian Shield, or the East Saharan Craton on the other side of the modern Red Sea. The
564 Arabian-Nubian Shield, that represents the closest area with unradiogenic material, is
565 composed of amalgamated juvenile oceanic arc terranes and ophiolite remnants, and of
566 reworked older crust and metasediments in the flanks of the shield, that formed the suture
567 between East and West Gondwana (Stern, 1994; Stein and Goldstein, 1996; Whitehouse et al.,
568 1998, 2001; Stern, 2002; Kusky and Li., 2003). The juvenile oceanic arc terranes and
569 ophiolite remnants, that compose the largest part of the shield, have ε_{Nd} values calculated at
570 80Ma typically between -5 to +18 ε-units (Duyverman et al., 1982; Johnson and
571 Woldehaimanot, 2003; Stoeser and Frost, 2006; Fig. 7; Suppl. Table 1). On the western flank
572 of the shield, a mix of juvenile and more ancient crust yield more variable and less radiogenic
573 ε_{Nd} values, down to -35 ε-unit at 80Ma (Harms et al., 1990, 1994; Stern, 1994; Johnson and
574 Woldehaimanot, 2003). The Khida terrane, that represents a small portion of a more ancient
575 continental crust, outcrops at present in the eastern part of the shield and yields the most

576 unradiogenic Nd isotope values of the Arabian Shield (ε_{Nd} values calculated at 80Ma ranging
577 between -23.8 and -6.3 ε-units; Fig. 7; Suppl. Table 1). Although quite far away from the
578 studied section, detrital material derived from these unradiogenic parts of the Arabian-Nubian
579 Shield may have been brought by rivers, in proportions that could have evolved in the context
580 of Africa-Eurasia convergence and associated tectonic movements, susceptible to modify
581 river catchment areas.

582 Interestingly, variations in detrital fraction $\varepsilon_{Nd(t)}$ present a striking temporal
583 coincidence with the evolution of clay mineralogical assemblages. More radiogenic $\varepsilon_{Nd(t)}$
584 values are recorded in the intervals rich in kaolinite while unradiogenic values are recorded
585 during intervals devoid of kaolinite and rich in chlorite and illite (Fig. 6). Wind-blown dust
586 can contribute significantly to the Nd isotope composition of the detrital material deposited in
587 oceanic basins (Grousset et al., 1988; Grousset and Biscaye, 2005). Along the western African
588 margin, markedly lower ε_{Nd} values (by up to +4 ε-units) have been recorded in the detrital
589 fraction of deep-sea core sediments deposited during the drier last glacial maximum,
590 compared to present-day values measured in core-tops at the same sites (Grousset et al.,
591 1988). These authors have interpreted these more unradiogenic values as deriving from
592 increasing inputs of Saharan wind-blown dust at these off-shore sites during the overall drier
593 climate interval corresponding to the Last Glacial Maximum. Similarly, the relatively
594 unradiogenic ε_{Nd} values recorded in the detrital fraction at Shahneshin may reflect to some
595 extent the presence of unradiogenic wind-blown dust mixed with radiogenic detrital material
596 derived from the weathering of nearby ophiolites and granitoids. The origin of this
597 unradiogenic dust would be difficult to determine, as it would be dependent of both
598 atmospheric circulation and of the location of deserts on ancient continental crust, but it may
599 have come from the East Saharan Craton, the Khida terrane, or, given the likely position of
600 the site relative to the trade-winds, from the Eurasian craton as much of south-east Asia is

thought to have been very dry during the late Cretaceous (Hasegawa et al., 2012). If this interpretation is correct, then the co-variations of kaolinite proportions in clay mineral assemblages with the ε_{Nd} values of the insoluble fraction would derive from significant variations in the contribution of this unradiogenic dust material. This contribution would have been higher in drier intervals marked by higher proportions of illite and chlorite, and lower in more humid intervals marked by higher proportions of kaolinite. The marked decrease in Nd isotope values of the insoluble fraction from the middle Campanian to the Maastrichtian, associated with high proportions of illite and chlorite, could thus reflect drier climatic conditions and an increased contribution of wind-blown unradiogenic material to the sediments of the section at that time.

5.4. An oceanic signal partially preserved?

The carbonate leachates all present a REE pattern typical of non-skeletal marine carbonates formed in shallow oxic seawater, with a negative Ce anomaly, a positive La anomaly, and an enrichment in heavy rare earth elements (Webb and Kamber, 2000; Tostevin et al., 2016). These REE patterns along with the significant difference, from 2 to over 4 ε-units recorded between the carbonate leachate and the residues ε_{Nd}, strongly suggest that the carbonate leachates record the ε_{Nd} of the local bottom seawater at Shahneshin.

It has been shown that on continental margins and proximal settings, local bottom seawater ε_{Nd} can be impacted by local detrital inputs, through processes called boundary exchanges (Lacan and Jeandel, 2001; Jeandel, 2016). Therefore, in such settings, the evolution of local seawater ε_{Nd} can be governed by changes in the source of the material eroded nearby. At Shahneshin, variations in local bottom seawater ε_{Nd} mirror that of the detrital fraction from the Coniacian to the middle Campanian. This co-variation strongly

626 suggests that changes in the Nd isotope composition of the sediments transported to the
627 Zagros Basin have likely driven the Nd isotope composition of the local seawater during this
628 interval. By contrast, a decoupling of both isotopic signals is depicted from the late
629 Campanian onward, highlighted by the increasing difference recorded between $\varepsilon_{Nd(t)bottom\ seawater}$ and $\varepsilon_{Nd(t)insoluble\ residue}$ from about 2 to over 4 ε-units ($\Delta\varepsilon_{Nd(t)\ boot.\ Sweater\ -\ insol\ resi}$; Fig. 6).
631 While the $\varepsilon_{Nd(t)}$ of the residue displays a marked decrease of about 3 ε-units from the middle
632 Campanian to the late Maastrichtian, the $\varepsilon_{Nd(t)}$ of the local bottom waters only shows a mild
633 decrease of less than 1 ε-unit on average. This difference points to increasing inputs of a
634 radiogenic water mass in the Zagros Basin during this interval, driving the Nd isotope
635 composition of the local seawater further away from the unradiogenic composition of the
636 nearby detrital supply. At that time, the only deep or intermediate water masses reported in
637 the literature with radiogenic compositions above -5 ε-units are water masses from the Pacific
638 Ocean ($\varepsilon_{Nd(t)}$ ranging between -7 and -3 ε-units during the Late Cretaceous; Thomas, 2004;
639 Hague et al., 2012; Thomas et al., 2014; Moiroud et al., 2016; Haynes et al., 2020).

640 During the Late Cretaceous, the large wind-driven westward flowing TCC flowed all
641 around the globe at low latitudes, from the Indian and Pacific Oceans into the Atlantic Ocean
642 through the Tethys, and then back to the Pacific through the Caribbean seaway (Winterer,
643 1991; Föllmi and Delamette, 1991; Otto-Bliesner et al., 2002; Donnadieu et al., 2006). The
644 development of upwellings along the southern Tethyan margin during the Campanian and
645 Maastrichtian, inferred from high productivity assemblages as radiolarites orrganic-matter
646 layers, and the occurrence of large phosphorite deposits (Salaj and Nairn, 1987 ; Föllmi et al.,
647 1992 ; Almogi-Labin et al., 1993 ; Pufahl et al., 2003 ; Lüning et al., 1998 ; Meilijson et al.,
648 2014 ; El-Shafeiy et al., 2014 ; Bou Daher et al., 2014, 2015), has been linked to an
649 intensification of the TCC at that time (Pucéat et al., 2005; Soudry et al., 2004, 2006). Our
650 new results thus support a more intense TCC in the late Campanian to Maastrichtian interval,

651 that would have resulted in enhanced inputs of radiogenic Pacific waters into the Zagros
652 Basin, driving the $\varepsilon_{Nd(t)}$ of the local seawater further away from that of the more unradiogenic
653 detrital inputs. Our work additionally suggests that the TCC could have extended to bathyal
654 depths during the Late Cretaceous, at least within the Zagros Basin.

655 Our results also highlight the quite radiogenic composition of bathyal waters in the
656 Zagros Basin, that display $\varepsilon_{Nd(t)}$ values in the range of -3.5 to -5.5 ε-units, about 2 to 3 ε-units
657 above the $\varepsilon_{Nd(t)}$ values of shallow waters of the Negev (Soudry et al., 2004, 2006). If such a
658 radiogenic composition is confirmed as a feature of bathyal waters in the eastern Tethys, the
659 development of an intense upwelling system could then have contributed to the increase in
660 shallow water $\varepsilon_{Nd(t)}$ values recorded in the Negev from the Turonian to the Campanian
661 (Soudry et al., 2004; 2006), along with the intensification of the TCC. More data from other
662 bathyal sites in the Tethys are however required to confirm the latter hypothesis.

663

664 ## 6. Conclusions

665

666 Our new clay mineralogical data coupled to sediment Ni/Al and Cr/Al ratios suggest
667 that the clay sedimentation of the eastern Tethys Shahneshin section was mainly driven by
668 changes in local hydrolysing conditions, potentially linked to global climatic change as
669 suggested by global records in benthic foraminifer $\delta^{18}O$. Humid intervals in the Coniacian to
670 Santonian and middle Campanian to early late Campanian periods could have favoured
671 kaolinite formation while more arid intervals (early Campanian and latest Campanian to late
672 Maastrichtian) would have inhibited kaolinite formation and promoted a higher proportion of
673 illite and chlorite in clay mineral assemblages.

674 The large increase recorded in sediment Ni/Al and Cr/Al from the upper Campanian
675 onward, that is not associated to a concomitant increase in the $\varepsilon_{Nd(t)}$ of the detrital fraction, is

interpreted as reflecting the alteration and erosion of the mantellic ultramafic material of the ophiolite sequence, that underlies basalt and gabbro. Following this interpretation, our data set imply that the ophiolite sequence was exposed to continental alteration and erosion in this area as soon as the Coniacian. Our results thus support a possible role of ophiolite obduction along the southern Tethyan margin in the Late Cretaceous long-term cooling through weathering of the exposed material, a process that draws down atmospheric CO_2.

The increasing difference recorded between the $\varepsilon_{Nd(t)}$ of the local bottom seawater and of the residue from the middle Campanian to the Maastrichtian points to a growing influence of a radiogenic water mass entering the Zagros Basin during this period. These results support an intensification of the westward flowing TCC during the Campanian and Maastrichtian that would have brought larger fluxes of radiogenic Pacific waters into the eastern Tethys. Our new data suggest that the TCC would have extended down to bathyal depth at that time, at least in the Zagros Basin. They also provide the first $\varepsilon_{Nd(t)}$ values of intermediate to deep waters within the Tethyan area revealing quite radiogenic values in this part of the eastern Tethys, in the range of -3.5 to -5.5 ε-units. Upwelling of such radiogenic waters onto the Negev platform during the Campanian and Maastrichtian could have partly contributed to the recorded increase in local seawater $\varepsilon_{Nd(t)}$ values at that time.

Acknowledgements

This research was funded by the ANR Anox-Sea coordinated by E. Pucéat. We would like to thank Marie-Laure Rouget, Emmanuel Ponzevera, Yoan Germain, Alexis de Prunelé and Philippe Telouk for their technical support in the geochemical analyses. M.J. Razmjooei and N. Thibault were funded by Carlsbergfondet CF16-0457. We are grateful to Thierry Adatte and an anonymous reviewer for constructive comments on the manuscript.

701

702 References

703

704 Adatte, T., Keller, G., Stinnesbeck, W., 2002. Late Cretaceous to early Paleocene climate and
705 sea-level fluctuations: the Tunisian record. *Palaeogeogr. Palaeoclimatol. Palaeoecol. 178*,
706 165–196.

707 Agar, R. A., Stacey, J.S., Whitehouse, M. J., 1992. Evolution of the southern Afif Terrane - a
708 geochronological study. *Saudi Arabian Directorate General of Mineral Resources*, 10–15.

709 Agard, P., Omrani, J., Jolivet, L., Mouthereau, F., 2005. Convergence history across Zagros
710 (Iran): constraints from collisional and earlier deformation. *Int. J. Earth Sci. 94*, 401–419.

711 Agard, P., Omrani, J., Jolivet, L., Whitechurch, H., Vrielynck, B., Spakman, W., Monié, P.,
712 Meyer, B., Wortel, R., 2011. Zagros orogeny: a subduction-dominated process. *Geol. Mag.*
713 *148*, 692–725.

714 Ahankoub, M., Jahangiri, A., Asahara, Y., Moayyed, M., 2013. Petrochemical and Sr-Nd
715 isotope investigations of A-type granites in the east of Misho, NW Iran. *Ara.b J. Geosci. 6*,
716 4833–4849.Ala, M.A., Kinghorn, R.R.F., Rahman, M.T., 1980. Organic geochemistry and
717 source rock characteristics of the Zagros petroleum province, southwest Iran. *J. Pet. Geol.*
718 *3*, 61–89.

719 Alavi, M., 1980. Tectonostratigraphic evolution of the Zagrosides of Iran. *Geology 8*, 144–
720 149.

721 Alavi, M., 1994. Tectonics of the Zagros orogenic belt of Iran: new data and interpretations.
722 *Tectonophysics 229*, 211–238.

723 Almogi-Labin, A., Bein, A., Sass, E., 1993. Late Cretaceous upwelling system along the
724 southern Tethys margin (Israel): interrelationship between productivity, bottom water
725 environments, and organic matter preservation. *Paleoceanography 8*, 671–690.

726 Alsenz, H., Regnery, J., Ashckenazi-Polivoda, S., Meilijson, A., Ron-Yankovich, L.,
727 Abramovich, S., Illner, P., Almogi-Labin, A., Feinstein, S., Berner, Z., 2013. Sea surface
728 temperature record of a Late Cretaceous tropical southern Tethys upwelling system.
729 *Palaeogeogr. Palaeoclimatol. Palaeoecol. 392*, 350–358.Ashckenazi-Polivoda, S.,
730 Abramovich, S., Almogi-Labin, A., Schneider-Mor, A., Feinstein, S., Püttmann, W.,
731 Berner, Z., 2011. Paleoenvironments of the latest Cretaceous oil shale sequence, Southern
732 Tethys, Israel, as an integral part of the prevailing upwelling system. *Palaeogeogr.*
733 *Palaeoclimatol. Palaeoecol. 305*, 93–108.

734 Ao, S., Xiao, W., Khalatbari Jafari, M., Talebian, M., Chen, L., Wan, B., Ji, W., Zhang, Z.,
735 2016. U–Pb zircon ages, field geology and geochemistry of the Kermanshah ophiolite
736 (Iran): From continental rifting at 79 Ma to oceanic core complex at ca. 36 Ma in the
737 southern Neo-Tethys. *Gondw. Research. 31*, 305–318.

738 Azizi, H., Hadi, A., Asahara, Y., Mohammad, Y.O., 2013. Geochemistry and geodynamics of
739 the Mawat mafic complex in the Zagros Suture zone, northeast Iraq. Central European *J. of*
740 *Geosci. 5*, 523–537.

741 Babaie, H., Babaei, A., Ghazi, A.M., Arvin, M., 2006. Geochemical, $^{40}Ar/^{39}Ar$ age, and
742 isotopic data for crustal rocks of the Neyriz ophiolite, Iran. *Canad. J. Earth Sci. 43*, 57–70.

743 Bárdossy, G., Dercourt, J., 1990. Les gisements de bauxites téthysiens (Méditerranée, Proche
744 et Moyen Orient); cadre paléogéographique et contrôles génétiques. *Bull. Soc. Géol.*
745 *France 6*, 869–888.

746 Barrat, J. A., Keller, F., Amossé, J., Taylor, R. N., Nesbitt, R. W., Hirata, T., 1996.
747 Determination of rare earth elements in sixteen silicate reference samples by ICP-MS after
748 Tm addition and ion exchange separation. *Geostandards News. 20*, 133–139.

749 Barrier, E., Vrielynck, B., 2007. Early Campanian (83 – 80.5 Ma). *In*: Palaeotectonic maps of
750 the Middle East, Atlas of maps; Tectono-Sedimentary-Palinspastic maps from Late Norian

751 to Pliocene. *Commission for the Geological Map of the World*, Paris.

752 Bayon, G., German, C.R., Boella, R.M., Milton, J.A., Taylor, R.N., Nesbitt, R.W., 2002. An
753 improved method for extracting marine sediment fractions and its application to Sr and Nd
754 isotopic analysis. *Chem. Geol. 187*, 179–199.

755 Bayon, G., Barrat, J.A., Etoubleau, J., Benoit, M., Bollinger, C., Révillon, S., 2009.
756 Determination of rare earth elements, Sc, Y, Zr, Ba, Hf and Th in geological samples by
757 ICP-MS after Tm addition and alkaline fusion. *Geostand. Geoanalyt. Research 33*, 51–62.

758 Bayon, G., Dennielou, B., Etoubleau, J., Ponzevera, E., Toucanne, S., Bermell, S., 2012.
759 Intensifying weathering and land use in iron age Central Africa. *Science 335***,** 1219–1222.

760 Beaufort, D., Rigault, C., Billon, S., Billault, V., Inoue, A., Inoue, S., Patrier, P. 2015.
761 Chlorite and chloritization processes through mixed-layer mineral series in lowtemperature
762 geological systems – a review. *Clay minerals 50*, 497–523.

763 Be'eri-Shlevin, Y., Katzir, Y., Blichert-Toft, J., Kleinhanns, I. C., Whitehouse, M. J., 2010.
764 Nd–Sr–Hf–O isotope provinciality in the northernmost Arabian–Nubian Shield:
765 implications for crustal evolution. *Contributions to Mineralogy and Petrology 160*, 181–
766 201.

767 Berberian, M., King, G.C.P., 1981. Towards a paleogeography and tectonic evolution of Iran.
768 *Canad. J. Earth Sci. 18*, 210–265.

769 Begemann, F., Kenneth, R.L., Lugmair, G.W., Walker, R.J., 2001. Call for improved set of
770 decay consants for geochronological use. *Geochim. Cosmochim. Acta 65*, 111–121.
771 Blusztajn, J., Hart, S.R., Shimizu, N., McGuire, A.V., 1995. Trace-element and isotopic
772 characteristics of spinel peridotite xenoliths from Saudi Arabia. *Chemi. Geol. 123*, 53-
773 65.Bokhari, F.Y., Kramers, J.D., 1981. Island-arc character and late Precambrian age of
774 volcanics at Wadi Shwas, Hijaz, Saudi Arabia: geochemical and Sr and Nd isotopic
775 evidence. *Earth Planet. Sci. Lett. 54*, 409–422.

776 Bornemann, A., Norris, R.D., Friedrich, O., Beckmann, B., Schouten, S., Sinninghe Damsté
777 J.S., Vogel, J., Hofmann, P., Wagner, T., 2008. Isotopic Evidence for Glaciation During
778 the Cretaceous Supergreenhouse. *Science 319*, 189–192.

779 Bosworth, W., Guiraud, R., Kessler, L.G., 1999. Late Cretaceous (ca. 84 Ma) compressive
780 deformation of the stable platform of northeast Africa (Egypt): Far-field stress effects of
781 the "Santonian event" and origin of the Syrian arc deformation belt. *Geology 27*, 633–636.

782 Bou Daher, S., Nader, F.H., Strauss, H., Littke, R., 2014. Depositional environment and
783 source-rock characterisation of organic-matter rich Upper Santonian–Upper Campanian
784 carbonates, northern Lebanon. *J. Petrol. Geol. 37*, 5–24.

785 Bou Daher, S.B., Nader, F.H., Müller, C., Littke, R., 2015. Geochemical and petrographic
786 characterization of Campanian–Lower Maastrichtian calcareous petroleum source rocks of
787 Hasbayya, South Lebanon. *Mar. Petrol. Geol. 64*, 304–323.Bouvier, A., Vervoort, J.D.,
788 Patchett, P.J., 2008. The Lu–Hf and Sm–Nd isotopic composition of CHUR: constraints
789 from unequilibrated chondrites and implications for the bulk composition of terrestrial
790 planets. *Earth Planet. Sci. Lett. 273*, 48–57.

791 Carignan, J., Hild, P., Mevelle, G., Morel, J., Yeghicheyan, D., 2001. Routine analyses of
792 trace elements in geological samples using flow injection and low pressure on-line liquid
793 chromatography coupled to ICP-MS: a study of geochemical reference materials BR, DR-
794 N, UB-N, AN-G and GH. *Geostandards Newsletter 25*, 187–198.

795 Chamley, H., 1989. Clay Sedimentology. Springer. Berlin, 623 pp.

796 Chamley, H., Bonnot-Courtois, C., 1981. Argiles authigènes et terrigènes de l'Atlantique et
797 du Pacifique. NW. *Oceanol. Acta 4*, 229–238.

798 Chamley, H., Deconinck, J-F., Millot, G., 1990. Sur l'abondance des minéraux smectitiques
799 dans les sédiments marins communs déposés lors des périodes de haut niveau marin du
800 Jurassique supérieur au Paléogène. *C R. Acad. Sci. Paris, Ser. II 311*, 1529–1536.

801 Chauvel., C., Blichert-Toft, J., 2001. A hafnium isotope and trace element perspective on
802 melting of the depleted mantle. *Earth Planet. Sci. Lett. 190*, 137–151.
803 Chenot, E., Pellenard, P., Martinez, M., Deconinck, J.-F., Amiotte-Suchet, P., Thibault, N.,
804 Bruneau, L., Cocquerez, T., Laffont, R., Pucéat, E., Robaszynski, F., 2016. Clay
805 mineralogical and geochemical expressions of the "Late Campanian Event" in the
806 Aquitaine and Paris basins (France): Palaeoenvironmental implications. *Palaeogeogr.*
807 *Palaeoclimatol. Palaeoecol. 447*, 42–52.
808 Chenot, E., Deconinck, J-F., Pucéat, E., Pellenard, P., Guiraud, M., Jaubert, M., Jarvis, I.,
809 Thibault, N., Cocquerez, T., Bruneau, L., Razmjooei, M.J., Boussaha, M., Richard, J.,
810 Sizun, J-P., Stemmerik, L., 2018. Continental weathering as a driver of Late Cretaceous
811 cooling: new insights from clay mineralogy of Campanian sediments from the southern
812 Tethyan margin to the Boreal realm, *Global Planet. Change 162*, 292–312.
813 Claesson, S., Pallister, J.S., Tatasumoto, M., 1984. Samarium-neodymium data on two late
814 Proterozoic ophiolites of Saudi Arabia and implications for crustal and mantle evolution.
815 *Contributions to Mineralogy and Petrology 85*, 244–252.
816 Cogné, J.-P., Humler, E., 2006. Trends and rhythms in global seafloor generation rate.
817 *Geochem. Geophys. Geosys. 7*, 1–17.
818 Darabi, G., Moghaddam, I.M., Sadeghi, A., Yusefi, B., 2018. Planktonic foraminifera and
819 sea-level changes in the upper Cretaceous of the Gurpi Formation, Lorestan basin, SW
820 Iran. *J. Afr. Earth Sci. 138*, 201–218.
821 Deconinck, J.-F., Chamley, H., 1995. Diversity of smectite origins in the Late Cretaceous
822 sediments: example of chalks from northern France. *Clay Miner. 30*, 365–380.
823 Delaloye, M., Desmons, J., 1980. Ophiolites and melange terranes in Iran: a geochronological
824 study and its paleotectonic implications. *Tectonophysics 68*, 83–111.
825 Dercourt, J., Zonenshain, L.P., Ricou, L.-E., Kazmin, V.G., Le Pichon, X., Knipper, A.L.,

826 Grandjacquet, C., Sbortshikov, I.M., Geyssant, J., Lepvrier, C., Pechersky, D.H., Boulin,
827 J., Sibuet, J.-C., Savostin, L.A., Sorokhtin, O., Westphal, M., Bazhenov, M.L., Lauer, J.P.,
828 Biju-Duval, B., 1986. Geological evolution of the tethys belt from the atlantic to the pamirs
829 since the LIAS. *Tectonophysics 123*, 241–315.

830 Donnadieu, Y., Goddéris, Y., Pierrehumbert, R., Dromart, G., Fluteau, F., Jacob, R., 2006. A
831 GEOCLIM simulation of climatic and biogeochemical consequences of Pangea breakup.
832 *Geochem. Geophy. Geosys. 7*, 1–21.

833 Dubinin, A.V., 2004. Geochemistry of rare earth elements in the ocean. *Lithology and mineral*
834 *resources 39*, 289–307.

835 Duyverman, H.J., Harris, N.B.W., Hawkesworth, C.J., 1982. Crustal accretion in the Pan
836 African: Nd and Sr isotope evidence from the Arabian Shield. *Earth Planet. Sci. Lett.* 59,
837 315–326.

838 El-Shafeiy, M., Birgel, D., El-Kammar, A., El-Barkooky, A., Wagreich, M., Mohamed, O.,
839 Peckmann, J., 2014. Palaeoecological and post-depositional changes recorded in
840 Campanian–Maastrichtian black shales, Abu Tartur plateau, Egypt. *Cret. Res. 50*, 38–51.

841 Eshet, Y., Almogi-Labin, A., 1996. Calcareous nannofossils as paleoproductivity indicators in
842 Upper Cretaceous organic-rich sequences in Israel. *Marine Micropal. 29*, 37–61.

843 Falzoni, F., Petrizzo, M.-R., Clarke, L.J., Macleod, K.G., Jenkyns, H.C., 2016. Long-term
844 Late Cretaceous oxygen- and carbon-isotope trends and planktonic foraminiferal turnover:
845 A new record from the southern midlatitudes. *GSA Bulletin 128*, 1725–1735.

846 Föllmi, K., B., Delamette, M., 1991. Model simulation of Mid-Cretaceous Ocean Circulation.
847 *Science 251*, pp. 94.

848 Föllmi, K.B., Garrison, R.E., Ramirez, P.C., Zambrano-Ortiz, F., Kennedy, W.J., Lehner,
849 B.L., 1992. Cyclic phosphate-rich successions in the upper Cretaceous of Colombia.
850 *Palaeogeogr. Palaeoclimatol. Palaeoecol. 93*, 151–182.

851 Frank, M., Whiteley, N., Kasten, S., Hein, J.R., O'Nions, K., 2002. North Atlantic Deep
852 Water export to the Southern Ocean over the past 14 Myr: Evidence from Nd and Pb
853 isotopes in ferromanganese crusts. *Paleoceanography 17,* 12-1–12-9.

854 Franks, P.J., Royer, D.L., Beerling, D.J., Van de Water, P.K., Cantrill, D.J., Barbour, M.M.,
855 Berry, J.A., 2014. New constraints on atmospheric CO_2 concentration for the Phanerozoic.
856 *Geophy. Res. Letters 41*, 4685–4694.

857 Friedrich, O., Norris, R.D., Erbacher, J., 2012. Evolution of middle to Late Cretaceous
858 oceans—A 55 my record of Earth's temperature and carbon cycle. *Geology 40*, 107–110.

859 Ghasemi, H., Juteau, T., Bellon, H., Sabzehi, M., Whitechurch, H., Ricou, L.E., 2002. The
860 mafic-ultramafic complex of Sikhoran (central Iran): a polygenetic ophiolite complex. *C.*
861 *R. Geosci. 334*, 431–438.

862 Giorgis, I., Bonetto, S., Giustetto, R., Lawane, A., Pantet, A., Rossetti, P., Thomassin, J.H.,
863 Vinai, R., 2014. The lateritic profile of Balkouin, Burkina Faso: Geochemistry, mineralogy
864 and genesis. *J. African. Earth Sciences. 90*, 31–48.

865 Goldstein, S.L., Hemming, S.R., 2003. Long-lived Isotopic Tracers in Oceanography,
866 Paleoceanography, and Ice-sheet Dynamics. *Treatise on Geochemistry 6*, 453–489.

867 Goldstein, S.L., O'Nions, R.K., Hamilton, P.J., 1984. A Sm-Nd isotopic study of atmospheric
868 dusts and particulates from major river systems. *Earth Planet. Sci. Lett. 70*, 221–236.

869 Govindaraju, K., 1995. 1995 working values with confidence limits for twenty-six CRPG,
870 ANRT and IWG-GIT geostandards. *Geostandards Newsletter 19*, 1–32.

871 Gradstein, F.M., Ogg, J.G., Schmitz, M., Ogg, G., 2012. The Geologic Time Scale 2012.
872 Elsevier, pp. 1176.

873 Grousset, F.E., Biscaye, P.E., 2005. Tracing dust sources and transport patterns using Sr, Nd
874 and Pb isotopes. *Chemi. Geol. 222*, 149–167.

875 Grousset, F.E., Biscaye, P.E., Zindler, A., Prospero, J., Chester, R., 1988. Neodymium
876 isotopes as tracers in marine sediments and aerosols: North Atlantic. *Earth Planet. Sci.*
877 *Lett. 87*, 367–378.

878 Guiraud, R., Bosworth, W., 1997. Senonian basin inversion and rejuvenation of rifting in
879 Africa and Arabia: synthesis and implications to plate-scale tectonics. *Tectonophysics 282*,
880 39–82.

881 Hague, A.M., Thomas, D.J., Huber, M., Korty, R., Woodard, S.C., Jones, L.B., 2012.
882 Convection of North Pacific deep water during the early Cenozoic. *Geology 40*, 527–530.

883 Harms, U., Schandelmeier, H., Darbyshire, D.P.F., 1990. Pan-African reworked early/middle
884 Proterozoic crust in NE Africa west of the Nile: Sr and Nd isotope evidence. *J. of the*
885 *Geological Soc. 147*, 859–872.

886 Harms, U., Darabyshire, D.P.F., Denkler, T., Hengst, M., Schandelmeier, H., 1994. Evolution
887 of the Neoproterozoic Delgo Suture zone and crustal growth in the Northern Sudan:
888 geochemical and radiogenic isotope constrains. *Geologische Rundschau 83*, 591–603.

889 Hasegawa, H., Tada, R., Jiang, X., Suganuma, Y., Imsamut, S., Charusiri, P., Ichinnorov, N.,
890 Khand, Y., 2012. Drastic shrinking of the Hadley circulation during the mid-Cretaceous
891 Supergreenhouse, Climate of the Past 8, 1323–1337.

892 Haynes, S.J., Macleod, K.G., Ladant, J.-B., Guchte, A.V., Rostami, M.A., Poulsen, C.J.,
893 Martin, E.E., 2020. Constraining sources and relative flow rates of bottom waters in the
894 Late Cretaceous Pacific Ocean. *Geology 48*, 509–513.

895 Hegner, E., Pallister, J.S., 1989. Pb, Sr, and Nd isotopic characteristics of Tertiary Red Sea
896 rift volcanics from the central Saudi Arabian coastal plain. *J. of Geophysical Research 94*,
897 7749–7755.

898 Hemmati-Nasab, M., Ghasemi-Nejad, E., Darvishzad, B., 2008. Paleobathymetry of the Gurpi
899 Formation based on benthic and planktonic foraminifera in Southwestern Iran. *J Sci.,*

900 *Islamic Republic of Iran 34*, 157–173.

901 Homke, S., Verges, J., Serra-Kiel, J., Bernaola, G., Sharp, I., Garces, M., Montero-Verdu, I.,
902 Karpuz, R., Goodarzi, M.H., 2009. Late Cretaceous-Paleocene formation of the proto-
903 Zagros foreland basin, Lurestan Province, SW Iran. *Geol. Soc. Am. Bull. 121*, 963–978.

904 Huber, B.T., Hodell, D.A., Hamilton, C.P., 1995. Middle-Late Cretaceous climate of the
905 southern high latitudes: stable isotopic evidence for minimal equator-to-pole thermal
906 gradients. *Geol. Soc. Am. Bull. 107,* 1164–1191.

907 Huber, B.T., Norris, R.D., Macleod, K.G., 2002. Deep-sea paleotemperature record of
908 extreme warmth during the Cretaceous. *Geology 30*, 123–126.

909 Huber, B.T., Macleod, K.G., Watkins, D. K., Coffin, M.F., 2018. The rise and fall of the
910 Cretaceous Hot Greenhouse climate. *Global Planet. Change 167*, 1–23.

911 Jagoutz, O., Macdonald, F.A., Royden, L., 2016. Low-latitude arc–continent collision as a
912 driver for global cooling. *PNAS 113*, 4935–4940.

913 Jeandel, C., 2016. Overview of the mechanisms that could explain the « Boundary
914 Exchange » at land-ocean contact. *Philosophical Transactions of the Royal Society A:*
915 *Mathematical, Physical and Engineering Sciences 374*.

916 Jochum, K. P., Weis, U., Schwager, B., Stoll, B., Wilson, S.A., Haug, G.H., Andreae, M.O.,
917 Enzweiler, J., 2016. Reference values following ISO Guidelines for frequently requested
918 rock reference materials. *Geostand. and Geoanal. Research 40*, 333–350.

919 Johnson, P.R., Woldehaimanot, B., 2003. Development of the Arabian-Nubian Shield:
920 perspectives on accretion and deformation in the northern East African Orogen and the
921 assembly of Gondwana. *Geological Society, London, Special Publications 206*, 289–325.

922 Jolivet, L., Faccenna, C., Agard, P., Frizon de Lamotte, D., Menant, A., Sternai, P.,
923 Guillocheau, F., 2016. Neo-Tethys geodynamics and mantle convection: from extension to

924 compression in Africa and a conceptual model for obduction. *Can. J. Earth Sci. 53*, 1190–
925 1204.

926 Karpoff, A.M., Destrigneville, C., Stille, P., 2007. Clinoptilolite as a new proxy of enhanced
927 biogenic silica productivity in lower Miocene carbonate sediments of the Bahamas
928 platform: Isotopic and thermodynamic evidence. *Chem. Geol. 245*, 285–304.

929 Keller, G., Adatte, T., Burns, S. J., Tantawy, A.A., 2002. High-stress palaeoenvironnmeent
930 during the late Maastrichtian to early Paleocene in Central Egypt. *Palaeogeogr.*
931 *Palaeoclimatol. Palaeoecol. 187,* 35–60.

932 Koop, W.J., Stoneley, R., 1982. Subsidence history of the Middle East Zagros Basin. *Phil.*
933 *Trans. Royal Soc. London 305*, 149–168.

934 Kröner, A., Linnebacher, P., Stern, R. J., Reischmann, T., Manton, W., Hussein, I. M., 1991.
935 Evolution of Pan-African island arc assemblages in the southern Red Sea Hills, Sudan and
936 in southwestern Arabia as exemplified by geochemistry and geochronology. *Precambrian*
937 *Research 53*, 99–118.

938 Koster, D., Liegeois, J.-E, 2001. Sr, Nd isotopes and geochemistry of the Bayuda Desert high-
939 grade metamorphic basement (Sudan): an early Pan-African oceanic convergent margin,
940 not the edge of the East Saharan ghost craton? *Precambrian Research 109*, 1–23.

941 Kusky, T.M., Li, J., 2003. Paleoproterozoic tectonic evolution of the North China Craton. *J.*
942 *of Asian Earth Sci. 22*, 383–397.

943 Lacan, F., Jeandel, C., 2001. Tracing Papua New Guinea imprint on the central Equatorial
944 Pacific Ocean using neodymium isotopic compositions and Rare Earth Element patterns.
945 *Earth Planet. Sci. Lett. 186*, 497–512.

946 Lanphere, M. A., Pamić, J., 1983. ^{40}Ar ^{39}Ar and tectonic setting of ophiolite from the Neyriz,
947 southeast Zagros Range, Iran. *Tectonophysics 96*, 245–256.

948 Linnert, C., Robinson, S.A., Lees, J.A., Brown, P.R., Pérez-Rodríguez, I., Petrizzo, M.R.,
949 Falzoni, F., Littler, K., Arz, J.A., Russell, E.E., 2014. Evidence for global cooling in the
950 Late Cretaceous. *Nat. Comm.*, 1–7.

951 Lugmair, G.W., Marti, K., 1977. Sm-Nd-Pu timepieces in the Angra dos Reis meteorite.
952 *Earth Planet. Sci. Lett. 35,* 273–284.

953 Lüning, S., Marzouk, A.M., Morsi, A.M., Kuss, J., 1998. Sequence stratigraphy of the Upper
954 Cretaceous of central-east Sinai, Egypt. *Cret.. Res. 19*, 153–195.

955 MacKay, C.B., Ansdell, K.M., 2013. Geochemical study of mafic and ultramafic rocks from
956 southern Hall Peninsula, Baffin Island, Nunavut. *In* Summary of Activities 2013, *Canada-*
957 *Nunavut Geoscience Office*, 85–92.

958 MacLeod, K.G., Londoño, C.I., Martin, E.E., Berrocoso, Á.J., Basak, C., 2011. Changes in
959 North Atlantic circulation at the end of the Cretaceous greenhouse interval. *Nat. Geosci. 4*,
960 779–782.

961 McKenzie, R., Horton, B.K., Loomis, S. E., Stockli, N.J., Planavsky, N.J., Lee, C.A., 2016.
962 Continental arc volcanism as the principal driver of icehouse-greenhouse variability,
963 *Science 352*, 444–447.

964 Meilijson, A., Ashckenazi-Polivoda, S., Ron-Yankovich, L., Illner, P., Alsenz, H., Speijer,
965 R.P., Almogi-Labin, A., Feinstein, S., Berner, Z., Püttmann, W., Abramovich, S., 2014.
966 Chronostratigraphy of the Upper Cretaceous high productivity sequence of the southern
967 Tethys, Israel. *Cret.. Res. 50*, 187–213.

968 Mills, B.J.W., Krause, A.J., Scotese, C.R., Hill, D.J., Shields, G.A., Lenton, T.M., 2019.
969 Modelling the long-term carbon cycle, atmospheric CO_2 and Earth surface temperature
970 from late Neoproterozoic to present day. *Gondw. Res. 67*, 172–186.

971 Moghazi, A. M., Andersen, T., Oweiss, G. A., Elbouse1ly, A. M., 1998. Geochemical and Sr-
972 Nd-Pb isotopic data bearing on the origin of Pan-African granitoids in the Kid area,

973 southeast Sinai, Egypt. *J. Geol. Soc., London 155*, 697–710.

974 Moiroud, M., Martinez, M., Deconinck, J.-F., Monna, F., Pellenard, P., Riquier, L.,
975 Compagny, M., 2012. High-resolution clay mineralogy as a proxy for orbital tuning:
976 example of the Hauterivian-Baremian transition in the Beltic Cordillera (SE Sapin).
977 *Sediment. Geol. 282*, 336–346.

978 Moiroud, M., Pucéat, E., Donnadieu, Y., Bayon, G., Guiraud, M., Voigt, S., Deconinck, J.-F.,
979 Monna, F., 2016. Evolution of neodymium isotopic signature of seawater during the Late
980 Cretaceous: Implications for intermediate and deep circulation. *Gondw. Res. 36*, 503–522.

981 Moore, D.M., Reynolds, R.C., 1997. X-Ray diffraction and the identification and analysis of
982 clay minerals, 2nd edition. (Eds.) Oxford University Press, Oxford, New York, pp. 378.

983 Monsef, I., Monsef, R., Mata, J., Zhang, Z., Pirouz, M., Rezaeian, M., Esmaeili, R., Xiao, W.,
984 2018. Evidence for an early-MORB to fore-arc evolution within the Zagros suture zone:
985 Constraints from zircon U-Pb geochronology and geochemistry of the Neyriz ophiolite
986 (South Iran). *Gondw. Res. 62*, 287–305.

987 Motiei, H., 1993. Stratigraphy of Zagros. Tehran: Geological Survey of Iran.

988 Murphy, D.P., Thomas, D.J., 2012. Cretaceous deep-water formation in the Indian sector of
989 the Southern Ocean: Cretaceous Deep-Water Circulation. *Paleoceanography 27*, 1–12.

990 Murphy, D.P., Thomas, D.J., 2013. The evolution of Late Cretaceous deep-ocean circulation
991 in the Atlantic basins: Neodymium isotope evidence from South Atlantic drill sites for
992 tectonic controls: Cretaceous Atlantic Deep Circulation. *Geochem. Geophys. Geosyst. 14*,
993 5323–5340.

994 Naderi, A., Ghasemi, H., Santos, J.F., Rocha, F., Griffin, W.L., Shafaii Moghadam, H.,
995 Papadopoulou, L., 2018. Petrogenesis and tectonic setting of the Tuyeh-Darvar Granitoid
996 (Northern Iran): Constraints from zircon U-Pb geochronology and Sr-Nd isotope
997 geochemistry. *Lithos 318*, 494–508.

998 Nouri, F., Asahara, Y., Azizi, H., Tsuboi, M., 2019. Petrogenesis of the Harsin–Sahneh
999 serpentinized peridotites along the Zagros suture zone, western Iran: new evidence for
1000 mantle metasomatism due to oceanic slab flux. *Geol. Magazine 156*, 772–800.

1001 Notholt, A.J.G., 1985. Phosphate resources in the Mediterranean (Tethyan) phosphogenic
1002 province: a progress report. *Sci. Geol. Memoire 77*, 9–21.

1003 O'Brien, C.L., Robinson, S.A., Pancost, R.D., Damsté, J.S.S., Schouten, S., Lunt, D.J.,
1004 Alsenz, H., Bornemann, A., Bottini, C., Brassell, S.C., Farnsworth, A., Forster, A., Huber,
1005 B.T., Inglis, G., Jenkyns, H. C., Linnert, C., Littler, K., Markwick, P., McAnena, A.,
1006 Mutterlose, J., Naafs, B.D.A., Püttmann, W., Sluijs, A., Van Helmond, N.A.G.M.,
1007 Vellekoop, J., Wagner, T., Wrobel, N.E., 2017. Cretaceous sea-surface temperature
1008 evolution: Constraints from TEX86 and planktonic foraminiferal oxygen isotopes. *Earth*
1009 *Sci. Rev. 172*, 224–247.

1010 Ogg, J.G., Ogg, G., Gradstein, F.M., 2016. A Concise Geologic Time Scale 2016. Elsevier.
1011 250 pages.

1012 Otto-Bliesner, B. L., Upchurch, G. R., 1997. Vegetation-induced warming of high latitude
1013 regions during the Late Cretaceous period. *Letters to nature 385*.

1014 Otto-Bliesner, B.L., Brady, E.C., Shields, C., 2002. Late Cretaceous ocean: Coupled
1015 simulations with the National Center for Atmospheric Research climate system model. *J.*
1016 *of Geophy. Res.: Atmospheres 107*, ACL–11–14.

1017 Petschick, R., 2000. MacDiff Ver. 4.2.6. Manual Geologisch-Palaontologisches Institute
1018 Johann Wolfgang Goethe Universitat Frankfurt Main senckenberganlage, 32–34.

1019 Philip, J., Floquet, M., 2000. Early Campanian (83 – 80.5 Ma). *In:* Crasquin, S. (Coord.),
1020 Atlas Peri-Tethys, Palaeogeographic maps. Explanatory notes. *Commission for the Geol.*
1021 *Map of the World*, Paris, 145–152.

1022 Pucéat, E., Lécuyer, C., Sheppard, S.M.F., Dromart, G., Reboulet, S., Grandjean, P., 2003.

1023 Thermal evolution of Cretaceous Tethyan marine waters inferred from oxygen isotope
1024 composition of fish tooth enamels. *Paleoceanography 18*, 1–12.
1025 Pucéat, E., Lécuyer, C., Reisberg, L., 2005. Neodymium isotope evolution of NW Tethyan
1026 upper ocean waters throughout the Cretaceous. *Earth Planet. Sci. Lett. 236*, 705–720.
1027 Pufahl, P.K., Grimm, K.A., Abed, A.M., Sadaqah, R.M.Y., 2003. Upper Cretaceous
1028 (Campanian) phosphorites in Jordan: implications for the formation of a south Tethyan
1029 phosphorite giant. *Sediment. Geol. 161*, 175–205.
1030 Razmjooei, M.J., Thibault, N., Kani, A., Mahanipour, A., Boussaha, M., Korte, C., 2014.
1031 Coniacian-Maastrichtian calcareous nannofossil biostratigraphy and carbon-isotope
1032 stratigraphy in the Zagros Basin (Iran): consequences for the correlation of the Late
1033 Cretaceous Stage Boundaries between the Tethyan and Boreal realms. *News. Stratigr. 47*,
1034 183–209.
1035 Razmjooei, M., Thibault, N., Kani, A., Dinarès-Turell, J., Pucéat, E., Shahriari, S.,
1036 Radmacher, W., Jamali, A.M., Ullmann, C.V., Voigt, S., Cocquerez, T., 2018. Integrated
1037 stratigraphy of the Late Cretaceous Gurpi Formation (Iran): a new reference for the eastern
1038 Tethys and implications for large-scale correlation of stage boundaries. *Cret. Res. 91*, 312–
1039 340.
1040 Razmjooei, M.J., Thibault, N., Kani, A., Ullmann, C.V. and Jamali, A.M., 2020a. Santonian-
1041 Maastrichtian carbon-isotope stratigraphy and calcareous nannofossil biostratigraphy of the
1042 Zagros Basin: Long-range correlation, similarities and differences of carbon-isotope trends
1043 at global scale. *Global Planet. Change 184*, 103075.
1044 Razmjooei, M.J., Thibault, N., Kani, A., Dinarès-Turell, J., Pucéat, E., Chin, S., 2020b.
1045 Calcareous nannofossil response to Late Cretaceous climate change in the eastern Tethys
1046 (Zagros Basin, Iran). *Palaeogeogr. Palaeoclimatol. Palaeoecol. 538*, 109418.
1047 Reischmann, T., Kröner, A., 1994. Late Proterozoic island arc volcanics from Gebeit, Red Sea

1048 Hills, northeast Sudan. *Geologische Rundschau 83*, 547–563.

1049 Revel, M., Ducassou, E., Grousset, F.E., Bernasconi, S.M., Migeon, S., Revillon, S., Mascle,
1050 J., Murat, A., Zaragosi, S., Bosch, D., 2010. 100,000 Years of African monsoon variability
1051 recorded in sediments of the Nile margin. *Quart. Sci. Rev. 29*, 1342–1362.

1052 Robinson, S.A., Murphy, D.P., Vance, D., Thomas, D.J., 2010. Formation of "Southern
1053 Component Water" in the Late Cretaceous: Evidence from Nd-isotopes. *Geology 38*, 871–
1054 874.

1055 Robinson, S.A., Vance, D., 2012. Widespread and synchronous change in deep-ocean
1056 circulation in the North and South Atlantic during the Late Cretaceous: Currents.
1057 *Paleoceanography 27*, 1–8.

1058 Rostami, M.A., Leckie, R.M., Font, E., Frontalini, F., Finkelstein, D., Koeberl, C., 2018. The
1059 Cretaceous-Paleogene transition at Galanderud (nothern Alborz, Iran): a multidisciplinay
1060 approach. *Palaeogeogr. Palaeoclimatol. Palaeoecol. 493*, 82–101.

1061 Royer, D.L., Pagani, M., Beerling, D.J., 2012. Geobiological constraints on Earth system
1062 sensitivity to CO_2 during the Cretaceous and Cenozoic. *Geobiology 10*, 298–310.

1063 Salaj, J., Nairn, A.E.M., 1987. Age and depositional environment of the Lower Tár "Member"
1064 of the Zimám Formation (Upper Senonian) in the Northern Hamada Al Hamra, Libya.
1065 *Palaeogeogr. Palaeoclimatol. Palaeoecol. 61*, 121–143.

1066 Saura, E., Verges, J., Homke, S., Blanc, E., Serra-Kiel, J., Bernaola, G., Casciello, E.,
1067 Fernandez, N., Romaire, I., Casini, G., Embry, J.C., Sharp, I.R., Hunt, D.W., 2011. Basin
1068 architecture and growth folding of the NW Zagros early foreland basin during the Late
1069 Cretaceous and early Tertiary. *J. Geol. Soc. London, 168*, 235–250.

1070 Saccani, E., Allahyari, K., Beccaluva, L., Bianchini, G., 2013. Geochemistry and petrology of
1071 the Kermanshah ophiolites (Iran): implication for the interaction between passive rifting,
1072 oceanic accretion, and OIB-type components in the southern Neo-Tethys Ocean. *Gondw.*

Res. 24, 392–411.

Schopka, H.H., Derry, L.A., Arcilla, C.A., 2011. Chemical weathering, river geochemistry and atmospheric carbon fluxes from volcanic and ultramafic regions on Luzon Island, the Philippines. *Geochim. Cosmochim. Acta 75*, 978–1002.

Şengör, A.C., Stock, J., 2014. The Ayyubid Orogen: an ophiolite obduction-driven orogen in the late Cretaceous of the Neo-Tethyan south margin. *Geosci. Canada 41*, 225–254.

Shafaii Moghadam, H., Stern, R.J., 2011. Geodynamical evolution of Upper Cretaceous Zagros ophiolites: formations of oceanic lithosphere above a nascent subduction zone. *Geol. Mag. 148*, 762–801.

Shafaii Moghadam, H., Stern, R., 2014. Ophiolites of Iran: Keys to understanding the tectonic evolution of SW Asia: (I) Paleozoic ophiolites. *J. of Asian Earth Sciences* 91, 19–38.

Shafaii Moghadam, H., Stern, R.J., 2015. Ophiolites of Iran: Keys to understanding the tectonic evolution of SW Asia: (II) Mesozoic ophiolites. *J. Asian Earth Sci.* 100, 31–59.

Shafaii Moghadam, H., Mosaddegh, H., Santosh, M., 2012. Geochemistry and petrogenesis of the Late Cretaceous Haji-Abad ophiolite (Outer Zagros Ophiolite Belt, Iran): implications for geodynamics of the Bitlis-Zagros suture zone. *Geol. J. 48.*

Shafaii Moghadam, H., Stern, R.J., Chiaradia, M., Rahgoshay, M., 2013. Geochemistry and tectonic evolution of the Late Cretaceous Gogher-Baft ophiolite, central Iran. *Lithos 16-169*, 33–47.

Shahidi, M., Nazari, H., 1997. Geological map of Harsin, 1/100.000 scale. Tehran: Geological survey of Iran.

Soudry, D., Segal, I., Nathan, Y., Glenn, C.R., Halicz, L., Lewy, Z., VonderHaar, D.L., 2004. $^{44}Ca/^{42}Ca$ and $^{143}Nd/^{144}Nd$ isotope variations in Cretaceous-Eocene Tethyan francolites and their bearing on phosphogenesis in the southern Tethys. *Geol. Soc. Amer. 32*, 389–392.

1097 Soudry, D., Glenn, C.R., Nathan, Y., Segal, I., Von der Haar, D., 2006. Evolution of Tethyan
1098 phosphogenesis along the northern edges of the Arabian–African shield during the
1099 Cretaceous–Eocene as deduced from temporal variations of Ca and Nd isotopes and rates
1100 of P accumulation. *Earth Sci. Rev. 78*, 27–57.

1101 Stacey, J.S., Hedge, C.E., 1984. Geochronologic and isotopic evidence for early Proterozoic
1102 crust in the eastern Arabian Shield. *Geology 12*, 310–313.

1103 Stein, M., Goldstein, S.L., 1996. From plume head to continental lithosphere in the Arabian–
1104 Nubian shield. *Nature 382*, 773–778.

1105 Stern, R.J., 1994. Arc assembly and continental collision in the Neoproterozoic East African
1106 Orogen: Implications for the assembly of Gondwana land. *Annual Rev. Earth Planet. Sci.*
1107 *22*, 319–351.

1108 Stern, R.J., 2002. Crustal evolution in the East African Orogen: a neodymium isotopic
1109 perspective. *J. Afri. Earth Sci. 34*, 109–117.

1110 Stern, R.J., Abdelsalam, M.G., 1998. Formation of juvenile continental crust in the Arabian-
1111 Nubian shield: evidence from granitic rocks of the Nakasib suture, NE Sudan. *Geologische*
1112 *Rundschau 87*, 150–160.

1113 Stoeser, D.B., Frost, C.D., 2006. Nd, Pb, Sr, and O isotopic characterization of Saudi Arabian
1114 shield terranes. *Chem. Geol. 226*, 163–188.

1115 Tanaka, T., Togashi, S., Kamioka, H., Amakawa, H., Kagami, H., Hamamoto, T., Yuhara, M.,
1116 Orihashi, Y., Yoneda, S., Shimizu, H., et al., 2000. JNdi-1: a neodymium isotopic
1117 reference in consistency with LaJolla neodymium. *Chem. Geol. 168*, 279–281.

1118 Tantawy, A.A., Keller, G., Adatte, T., Stinnesbeck, W., Kassab, A., Schulte, P., 2001.
1119 Maastrichtian to Paleocene depositional environnement of the Dakhla Formation, Western
1120 Desert, Egypt: sedimentology, mineralogy and integrated micro- and macrofossil
1121 biostratigraphies. *Cret. Res. 22*, 795–827.

1122 Taylor, S.R., McLennan, S.M., 1985. The continental crust: its composition and evolution.
1123 Blackwell, Oxford, pp. 312.

1124 Tessier, A., Campbell, P.G.C., Bisson, M., 1979. Sequential extraction procedure for the
1125 speciation of particulate trace metals. *Analytical Chem. 51*, 844–851.

1126 Tilton, G.R., Hopson, C.A., Wright, J.E., 1981. Uranium-lead isotopic ages of the Samail
1127 Ophiolite, Oman, with applications to Tethyan ocean ridge tectonics. *J. Geophy. Res. Solid*
1128 *Earth 86*, 2763–2775.

1129 Thiry, M., Jacquin, T., 1993. Clay mineral distribution related to rift activity, sea-level
1130 changes and paleoceanography in the Cretaceous of the Atlantic Ocean. *Clay Min. 28*, 61–
1131 84.

1132 Thomas, D.J., 2004. Evidence for deep-water production in the North Pacific Ocean during
1133 the early Cenozoic warm interval. *Nature 430*, 65–68.

1134 Thomas, D.J., Korty, R., Huber, M., Schubert, J.A., Haines, B., 2014. Nd isotopic structure of
1135 the Pacific Ocean 70–30 Ma and numerical evidence for vigorous ocean circulation and
1136 ocean heat transport in a greenhouse world. *Paleoceanography 29*, 454–469.ope
1137 paleothermometry. *Geology 42*, 351–354.

1138 Tostevin, R., Shields, G.A., Tarbuck, G.M., He, T., Clarkson, M.O., Wood, R.A., 2016.
1139 *Chem. Geol. 438*, 146–162.

1140 Upchurch, G. R., Kiehl, J., Schields, C., Scherer, J., Scotese, C., 2015. Latitudinal
1141 temperature gradients and high-latitude temperatures during the latest Cretaceous:
1142 congruence of geological data and climate models. *Geology 43*, 683–689.

1143 Vanderaveroet, P., Averbuch, O., Deconinck, J.-F., Chamley, H., 1999. A record of
1144 glacial/interglacial alternations in Pleistocene sediments off New Jersey expressed by clay
1145 mineral, grain-size and magnetic susceptibility data. *Marine Geology 159*, 79–92.

1146 Van der Meer, D.G., Zeebe, R., Van Hisbergen, D.J.J., Sluijs, A., Sparkman, W., Torsvik,
1147 T.H., 2014. Plate tectonic controls on atmospheric CO_2 levels since the Triassic. *Proc.*
1148 *Natl. Acad. Sci. U.S.A.* 111, 4380–4385.

1149 Van der Lubbe, H.J.L., Franck, M., Tjallingii, R., Schneider, R.R., 2016. Neodymium isotope
1150 constraints on provenance, dispersal, and climate-driven supply of Zambezi sediments
1151 along the Mozambique Margin during the past ~45,000 years. *Geochem. Geophy. Geosys.*
1152 *17*, 181–198.

1153 Voigt, S., Jung, C., Friedrich, O., Frank, M., Teschner, C., Hoffmann, J., 2013. Tectonically
1154 restricted deep-ocean circulation at the end of the Cretaceous greenhouse. *Earth Planet.*
1155 *Sci. Lett. 369–370*, 169–177.

1156 Wang, Y., Huang, C., Sun, B., Quan, C., Wu, J., Lin, Z., 2014. Paleo-CO_2 variation trends
1157 and the Cretaceous greenhouse climate. *Earth Sci. Rev. 129*, 136–147.

1158 Webb, G.E., Kamber, B.S., 2000. Rare earth elements in Holocene reefal microbialites: a new
1159 shallow seawater proxy. *Geochim. Cosmochim. Acta 9*, 1557–1565.

1160 Whitechurch, H., Omrani, J., Agard, P., Humbert, F., Montingny, R., Jolivet, L., 2013.
1161 Evidence for Paleocene-Eocene evolution of the foot of the Eurasian margin (Kermashah
1162 ophiolite, SW Iran) from back-arc to arc: implications for regional geodynamics and
1163 obduction. *Lithos 182 – 183*, 11–32.

1164 Whitehouse, M.J., Windley, B.F., Ba-Batt, M.A.O., Faning, C.M., Rex, D.C., 1998. Crustal
1165 evolution and terrane correlation in the eastern Arabian Shield, Yemen: geochronological
1166 constraints. *J. Geol. Soc. 155*, 281–296.

1167 Whitehouse, M.J., Windley, B.F., Stoeser, D.B., Al-Khirbash, S., Ba-Bttat, M.A., Haider, A.,
1168 2001. Precambrian basement character of Yemen and correlations with Saudi Arabia and
1169 Somalia. *Precamb. Res. 105*, 357–369.

1170 Weis, D., Kieffer, B., Maerschalk, C., Barling, J., de Jong, J., Williams, G.A., Hanano, D.,

1171 Pretorius, W., Mattielli, N., Scoates, J.S., 2006. High-precision isotopic characterization of
1172 USGS reference materials by TIMS and MC-ICP-MS. *Geochem. Geophy. Geosys. 7*, 1–30.
1173 Wilson, D.J., Piotrowski, A.M., Galy, A., Clegg, J.A., 2013. Reactivity of neodymium
1174 carriers in deep sea sediments: Implications for boundary exchange and paleoceanography.
1175 *Geochim. Cosmochim. Acta 109*, 197–221.
1176 Winterer, E.L., 1991. The Tethyan Pacific during Late Jurassic and Cretaceous times.
1177 *Palaeogeogr. Palaeoclimatol. Palaeoecol 87*, 253–265.
1178 Zarei, E., Ghasemi-Nejad, E., 2015. Sequence stratigraphy of the Gurpi Formation
1179 (Campanian–Paleocene) in southwest of Zagros, Iran, based on palynomorphs and
1180 foraminifera. *Arab. J. Geosci. 8*, 4011–4023.

1181 Figures and Tables

1182

1183 Figure 1: Structural map of the western Iranian domain (modified from Homke et al., 2009)
1184 replaced on a google earth picture (A), palaeogeographical maps of the eastern Tethyan
1185 Realm during the early Campanian (B) and late Maastrichtian (C; modified from Barrier and
1186 Vrielynck, 2007). Abbreviations: TCC = Tethyan Circum global Current; *Zag. Bas.* = Zagros
1187 Basin.

1188 Figure 2: Field view of the Shahneshin section (Zagros Basin, Iran) (A) uppermost Santonian
1189 to lowemost Campanian stratigraphic succession and (B) upper Campanian stratigraphic
1190 succession.

1191 Figure 3: Clay mineralogy of the Shahneshin section compared with the $\varepsilon_{Nd(t)}$ of the acetic
1192 acid leachates and of the insoluble fractions, and with the Ni/Al [(Ni(ppm)/Al(%))x10 000]
1193 and Cr/Al [(Cr(ppm)/Al(%)x10 000] ratios. These data have been replaced along the
1194 lithological succession, the calcareous nannofossils and planktonic foraminifera
1195 biostratigraphy and the $\delta^{13}C$ bulk rock curve of Razmjooei et al. (2018). The 2σ error are 0.35
1196 ε-units for the insoluble fraction and 0.21 ε-units for the acetic acid leachate fraction.
1197 Abbreviations: C = Coniacian ; Maast. = Maastrichtian ; Sa = Santonian

1198 Figure 4: X-ray diffractograms of the clay fraction of some samples from the Shahneshin
1199 section, at 81m, 234m and 313m. The comparison of the X-ray diffractograms below 250 m
1200 (at 81m and 234m) and above 250 m (at 313m) highly suggests the presence of vermiculite
1201 with high and narrow 14Å peak in the upper part of the section. This difference reflects the
1202 probable occurrence of vermiculite.

1203 Figure 5: PAAS-normalized REE patterns for acetic acid leachates (at the top) and insoluble
1204 fractions (at the bottom) of the Shahneshin samples.

1205 Figure 6: Evolution of the proportions of illite, chlorite and kaolinite compared with $\varepsilon_{Nd(t)}$ of

the local bottom seawater and of the insoluble fraction at Shahneshin, and the Ni/Al and Cr/Al ratios, during the Late Cretaceous. The relative ages have been calculated using the new age-model established for the Shahneshin section (see Table 1 and Suppl. Fig. 1., modified from Razmjooei et al., 2018, based on GTS 2016 from Ogg et al., 2016). The 2σ error are 0.35 ε-units for the insoluble fraction and 0.21 ε-units for the local bottom seawater. $\Delta\varepsilon_{Nd(t)}$ represent the difference between $\varepsilon_{Nd(t)}$ of the seawater and the insoluble fraction. TEX86 palaeotemperature data are from Pama quarry (Israel), Adrehet 1 borehole (Israel; Alsenz et al., 2013) and Shulqualak-Evans borehole (Linnert et al., 2014) and $\delta^{18}O_{planktonic\ foraminifera}$ palaeotemperature data from ODP Site 1259 (Bornemann et al., 2008), ODP Site 1050 (Huber et al., 2002; O'Brien et al., 2017) and ODP Site 762 (Falzoni et al., 2016). These palaeo sea surface temperature are replaced along age model from O'Brien et al. (2017), based on GTS 2012 (Gradstein et al., 2012)

Figure 7: Nd isotopic composition (ε_{Nd}) calculated at 80Ma (references and calculation in Suppl. Table 1) of different magmatic complexes outcropping in the general area of the Zagros Basin. Present-day extension of the Arabian-Nubian Shield (dark grey), terrane delimitation, and Precambrian deposition basins (dashed outline) from Johnson and Woldehaimanot (2003).

Abbreviations: EG = Eastern Gulf Basin; F = Fahud Basin; G = Ghudun Basin; Gh = Ghaba Basin; SO = South Oman Basin; WG = Western Gulf Basin. The hatched area corresponds to the western oceanic arc, and the dotted area to the eastern oceanic arc, as defined in Stoeser and Frost (2006).

Table 1: Eight anchor points used to build the age-model for the Shahneshin section (updated from Razmjooei et al., 2018 taking into account the new results on Bowan section presented in Razmjooei et al., 2020a).

Table 2: REE concentrations and Nd isotopic data of the insoluble fraction, the acetic acid

leachate of the Shahneshin section and the certified reference material used in the analytic series. $\varepsilon_{Nd(t)}$ values of the Shahneshin section's samples have been calculated using the age-model of Table 1.

Table 2: Bulk rock major and trace element concentrations of the samples from the Shahneshin section.

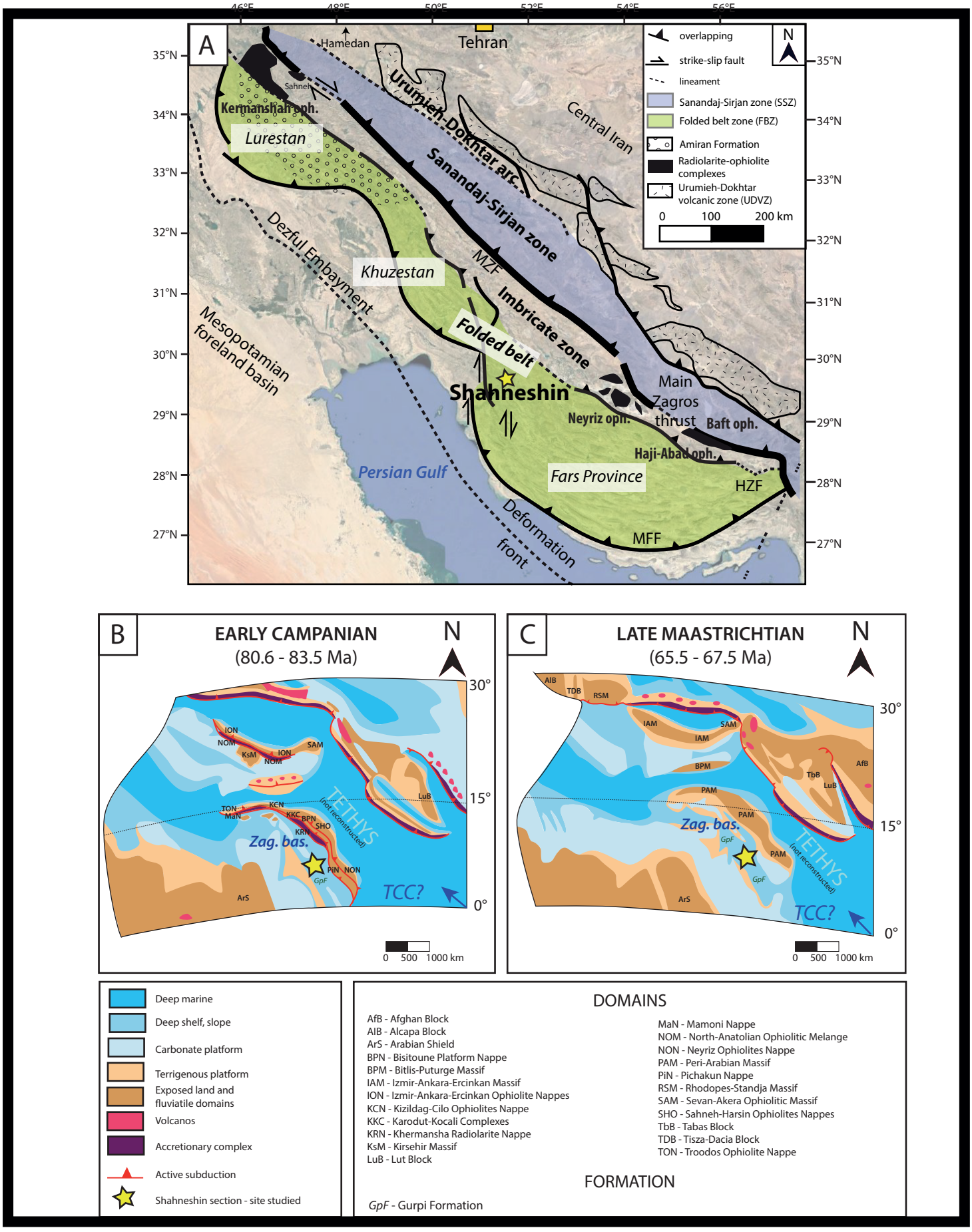
A
Hamedan
Tehran
Sahneh
Kermanshah oph.
Lurestan
Urumieh-Dokhtar arc
Sanandaj-Sirjan zone
Central Iran
Dezful Embayment
Khuzestan
MZF
Imbricate zone
Folded belt
Shahneshin
Mesopotamian foreland basin
Persian Gulf
Neyriz oph.
Main Zagros thrust
Baft oph.
Haji-Abad oph.
Fars Province
HZF
MFF
Deformation front
overlapping
strike-slip fault
lineament
Sanandaj-Sirjan zone (SSZ)
Folded belt zone (FBZ)
Amiran Formation
Radiolarite-ophiolite complexes
Urumieh-Dokhtar volcanic zone (UDVZ)
0 100 200 km
N
46°E
48°E
50°E
52°E
54°E
56°E
35°N
34°N
33°N
32°N
31°N
30°N
29°N
28°N
27°N
B
EARLY CAMPANIAN
(80.6 - 83.5 Ma)
ION
NOM
KsM
SAM
KCN
MaN
KKC
BPN
SHO
KRN
Zag. bas.
PiN
NON
GpF
ArS
TCC?
LuB
TETHYS
(not reconstructed)
30°
15°
0°
0 500 1000 km
C
LATE MAASTRICHTIAN
(65.5 - 67.5 Ma)
AlB
TDB
RSM
IAM
SAM
BPM
PAM
TbB
AfB
LuB
Zag. bas.
GpF
ArS
TCC?
TETHYS
(not reconstructed)
30°
15°
0°
0 500 1000 km
Deep marine
Deep shelf, slope
Carbonate platform
Terrigenous platform
Exposed land and fluviatile domains
Volcanos
Accretionary complex
Active subduction
Shahneshin section - site studied
DOMAINS
AfB - Afghan Block
AlB - Alcapa Block
ArS - Arabian Shield
BPN - Bisitoune Platform Nappe
BPM - Bitlis-Puturge Massif
IAM - Izmir-Ankara-Ercinkan Massif
ION - Izmir-Ankara-Ercinkan Ophiolite Nappes
KCN - Kizildag-Cilo Ophiolites Nappe
KKC - Karodut-Kocali Complexes
KRN - Khermansha Radiolarite Nappe
KsM - Kirsehir Massif
LuB - Lut Block
MaN - Mamoni Nappe
NOM - North-Anatolian Ophiolitic Melange
NON - Neyriz Ophiolites Nappe
PAM - Peri-Arabian Massif
PiN - Pichakun Nappe
RSM - Rhodopes-Standja Massif
SAM - Sevan-Akera Ophiolitic Massif
SHO - Sahneh-Harsin Ophiolites Nappes
TbB - Tabas Block
TDB - Tisza-Dacia Block
TON - Troodos Ophiolite Nappe
FORMATION
GpF - Gurpi Formation

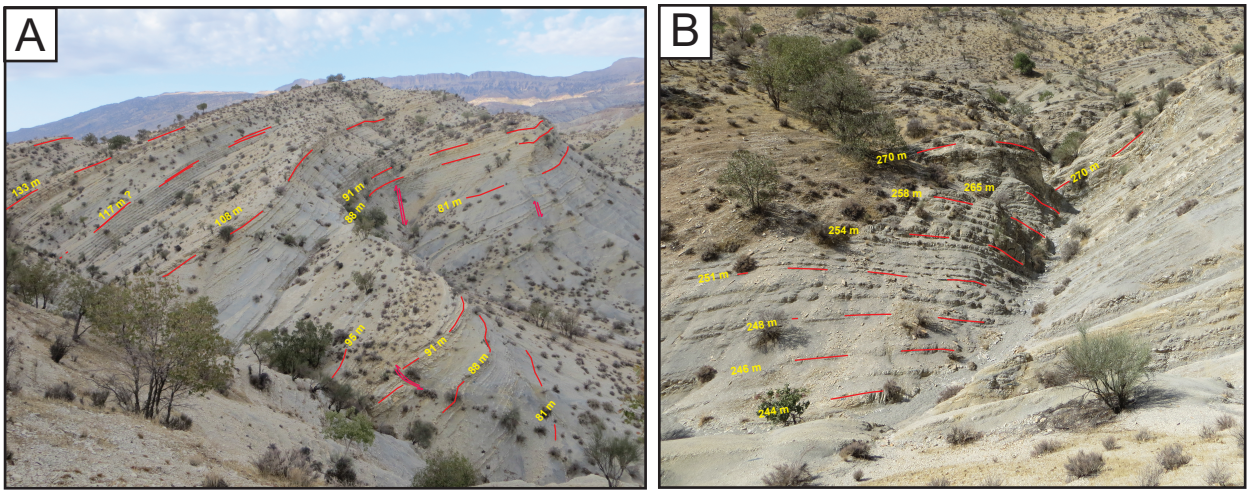
A
153 m
117 m ?
108 m
91 m
69 m
81 m
91 m
91 m
69 m
91 m
B
270 m
258 m
265 m
210 m
254 m
251 m
248 m
246 m
244 m

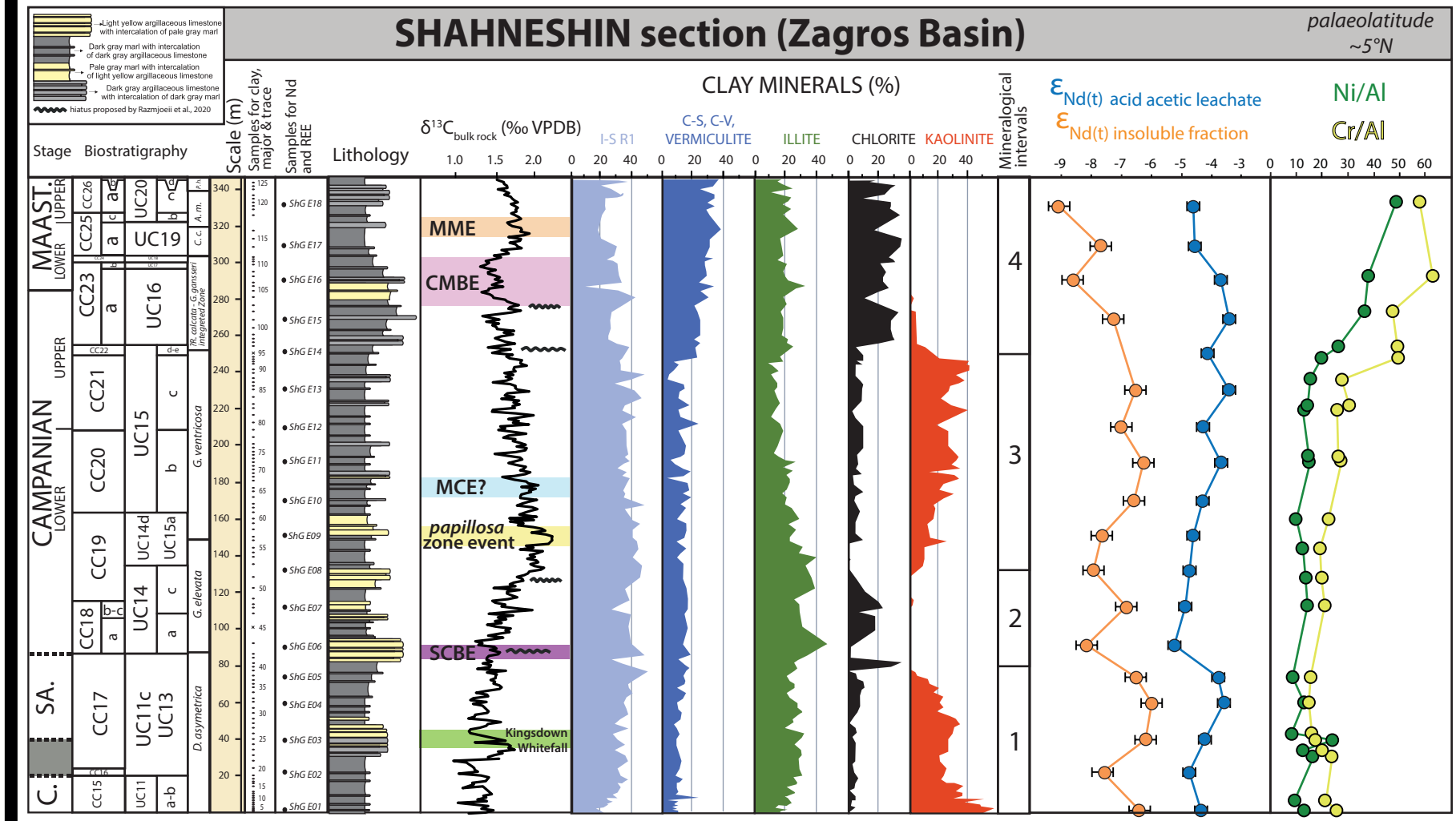
SHAHNESHIN section (Zagros Basin)
palaeolatitude ~5°N
Light yellow argillaceous limestone with intercalation of pale gray marl
Dark gray marl with intercalation of dark gray argillaceous limestone
Pale gray marl with intercalation of light yellow argillaceous limestone
Dark gray argillaceous limestone with intercalation of dark gray marl
hiatus proposed by Razmjoeii et al., 2020
Stage
Biostratigraphy
Scale (m)
Samples for clay, major & trace
Samples for Nd and REE
Lithology
δ13Cbulk rock (‰ VPDB)
CLAY MINERALS (%)
I-S R1
C-S, C-V, VERMICULITE
ILLITE
CHLORITE
KAOLINITE
Mineralogical intervals
εNd(t) acid acetic leachate
εNd(t) insoluble fraction
Ni/Al
Cr/Al
MME
CMBE
MCE?
papillosa zone event
SCBE
Kingsdown Whitefall
MAAST. UPPER
LOWER
CAMPANIAN UPPER
LOWER
SA.
C.
G. ventricosa
G. elevata
D. asymetrica

Sample Depth (meters)	Raw Diffractogram	Interpreted Diffractogram
81	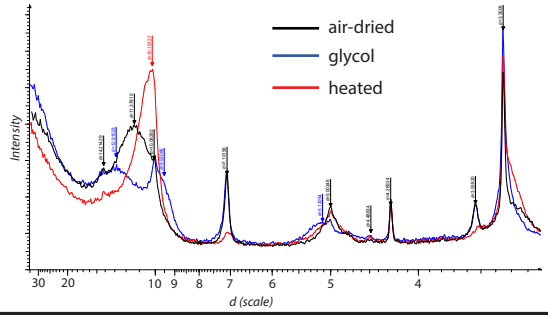	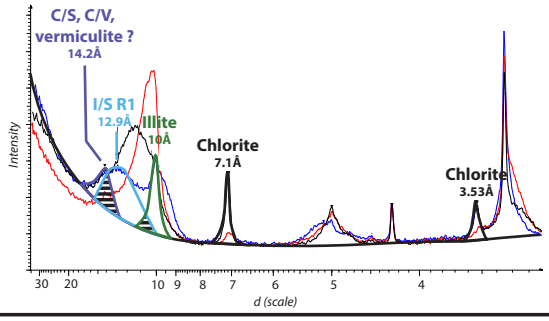
234	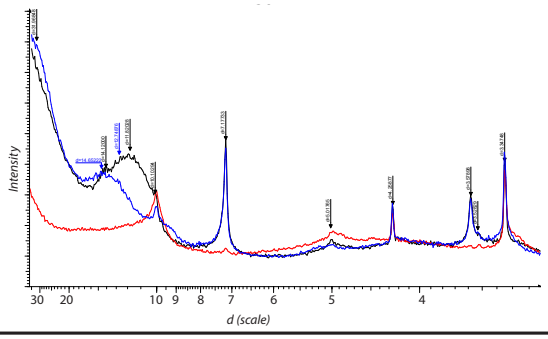	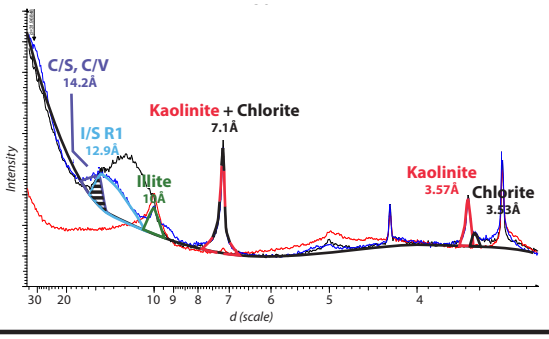
313	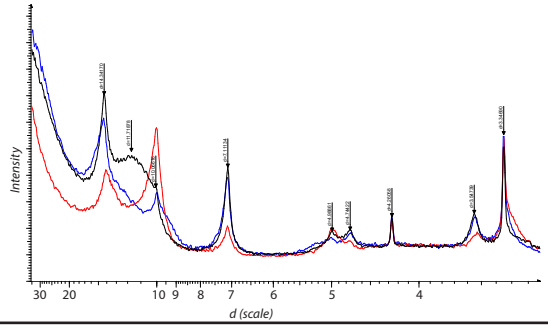	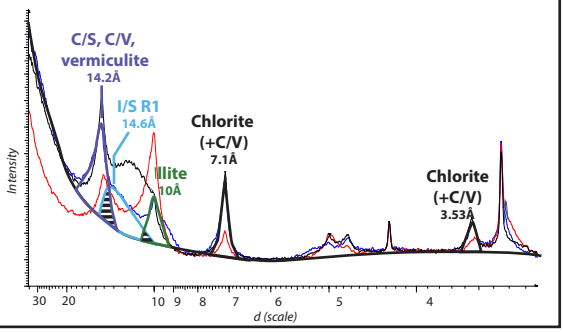

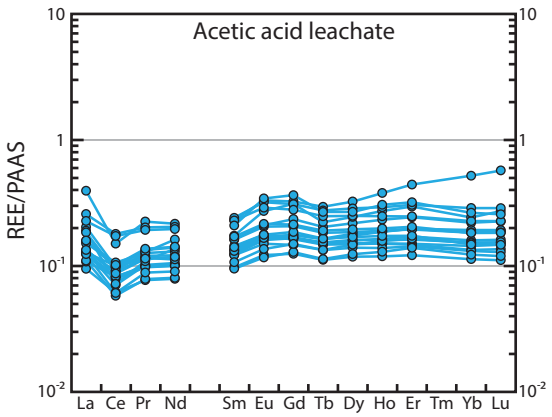
Acetic acid leachate
REE/PAAS
10
1
10^{-1}
10^{-2}
La Ce Pr Nd Sm Eu Gd Tb Dy Ho Er Tm Yb Lu

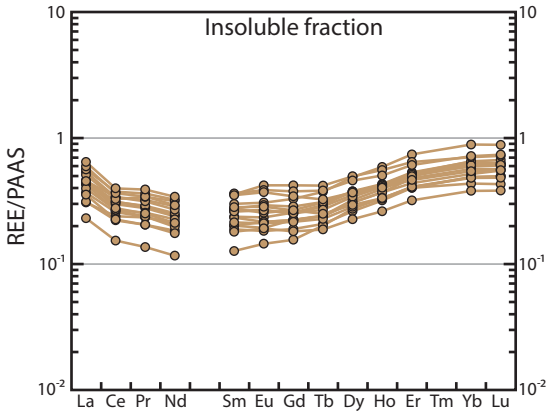
Insoluble fraction
REE/PAAS
10
1
10^{-1}
10^{-2}
La Ce Pr Nd Sm Eu Gd Tb Dy Ho Er Tm Yb Lu

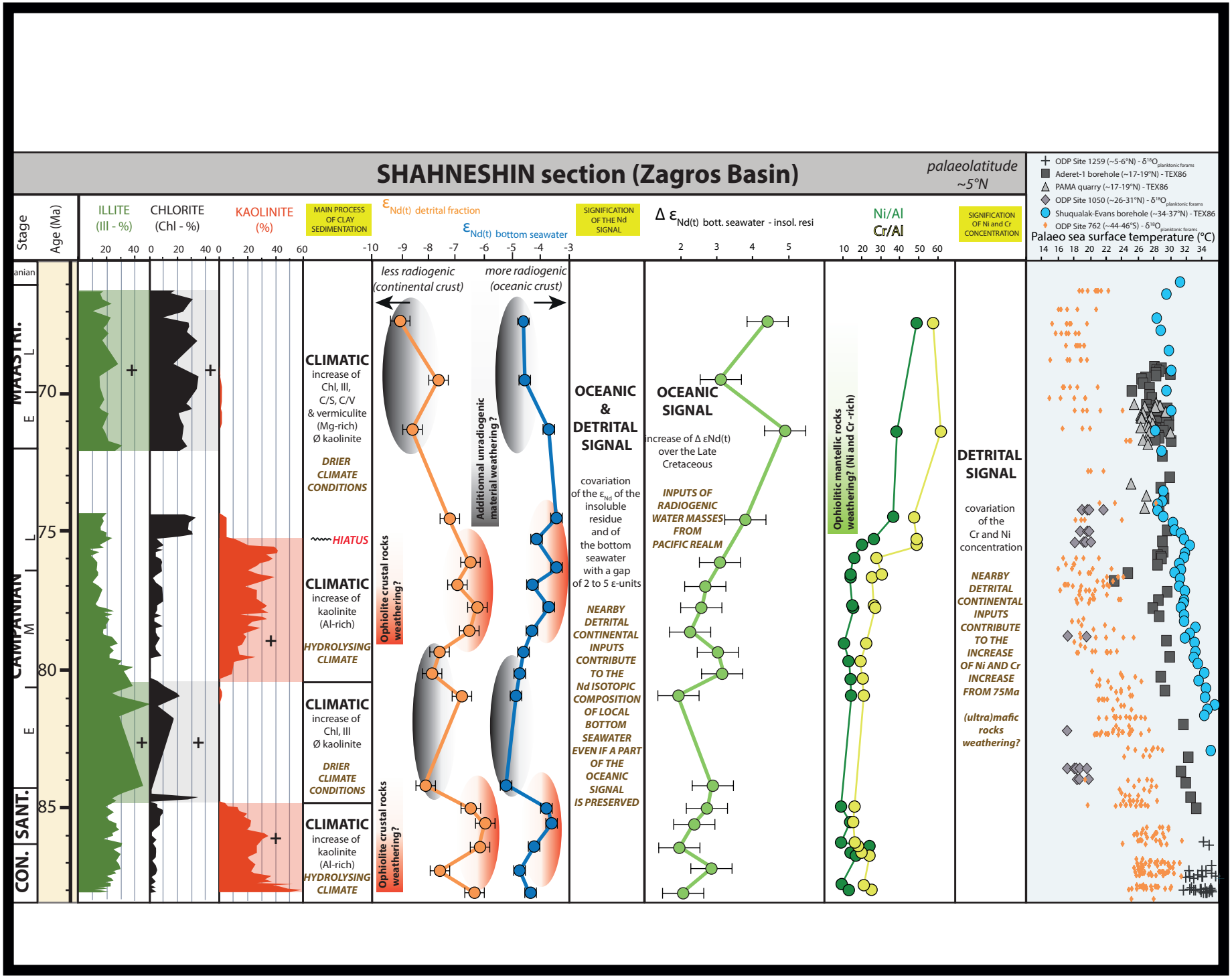
SHAHNESHIN section (Zagros Basin)
palaeolatitude ~5°N
Stage
Age (Ma)
ILLITE (Ill - %)
CHLORITE (Chl - %)
KAOLINITE (%)
MAIN PROCESS OF CLAY SEDIMENTATION
εNd(t) detrital fraction
εNd(t) bottom seawater
SIGNIFICATION OF THE Nd SIGNAL
Δ εNd(t) bott. seawater - insol. resi
Ni/Al
Cr/Al
SIGNIFICATION OF Ni and Cr CONCENTRATION
ODP Site 1259 (~5-6°N) - δ18Oplanktonic forams
Aderet-1 borehole (~17-19°N) - TEX86
PAMA quarry (~17-19°N) - TEX86
ODP Site 1050 (~26-31°N) - δ18Oplanktonic forams
Shuqualak-Evans borehole (~34-37°N) - TEX86
ODP Site 762 (~44-46°S) - δ18Oplanktonic forams
Palaeo sea surface temperature (°C)
MAASTRI.
CAMPANIAN
SANT.
CON.
70
75
80
85
less radiogenic (continental crust)
more radiogenic (oceanic crust)
Additionnal unradiogenic material weathering ?
Ophiolite crustal rocks weathering?
CLIMATIC increase of Chl, Ill, C/S, C/V & vermiculite (Mg-rich) Ø kaolinite
DRIER CLIMATE CONDITIONS
HIATUS
CLIMATIC increase of kaolinite (Al-rich)
HYDROLYSING CLIMATE
CLIMATIC increase of Chl, Ill Ø kaolinite
DRIER CLIMATE CONDITIONS
CLIMATIC increase of kaolinite (Al-rich)
HYDROLYSING CLIMATE
OCEANIC & DETRITAL SIGNAL
covariation of the εNd of the insoluble residue and of the bottom seawater with a gap of 2 to 5 ε-units
NEARBY DETRITAL CONTINENTAL INPUTS CONTRIBUTE TO THE Nd ISOTOPIC COMPOSITION OF LOCAL BOTTOM SEAWATER EVEN IF A PART OF THE OCEANIC SIGNAL IS PRESERVED
OCEANIC SIGNAL
increase of Δ εNd(t) over the Late Cretaceous
INPUTS OF RADIOGENIC WATER MASSES FROM PACIFIC REALM
Ophiolitic mantellic rocks weathering? (Ni and Cr -rich)
DETRITAL SIGNAL
covariation of the Cr and Ni concentration
NEARBY DETRITAL CONTINENTAL INPUTS CONTRIBUTE TO THE INCREASE OF Ni AND Cr INCREASE FROM 75Ma
(ultra)mafic rocks weathering?

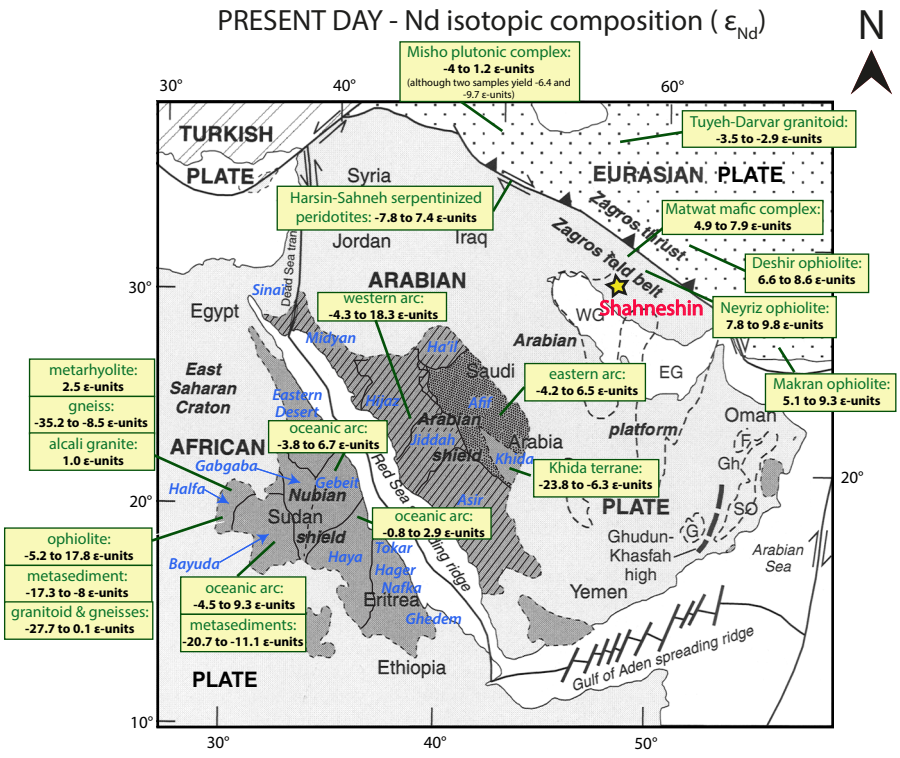
PRESENT DAY - Nd isotopic composition (εNd)
N
Misho plutonic complex:
-4 to 1.2 ε-units
(although two samples yield -6.4 and -9.7 ε-units)
Tuyeh-Darvar granitoid:
-3.5 to -2.9 ε-units
Harsin-Sahneh serpentinized peridotites: -7.8 to 7.4 ε-units
Matwat mafic complex:
4.9 to 7.9 ε-units
Deshir ophiolite:
6.6 to 8.6 ε-units
Neyriz ophiolite:
7.8 to 9.8 ε-units
Makran ophiolite:
5.1 to 9.3 ε-units
western arc:
-4.3 to 18.3 ε-units
eastern arc:
-4.2 to 6.5 ε-units
oceanic arc:
-3.8 to 6.7 ε-units
Khida terrane:
-23.8 to -6.3 ε-units
oceanic arc:
-0.8 to 2.9 ε-units
oceanic arc:
-4.5 to 9.3 ε-units
metasediments:
-20.7 to -11.1 ε-units
metarhyolite:
2.5 ε-units
gneiss:
-35.2 to -8.5 ε-units
alcali granite:
1.0 ε-units
ophiolite:
-5.2 to 17.8 ε-units
metasediment:
-17.3 to -8 ε-units
granitoid & gneisses:
-27.7 to 0.1 ε-units
TURKISH PLATE
EURASIAN PLATE
ARABIAN PLATE
AFRICAN PLATE
Syria
Jordan
Iraq
Egypt
Saudi Arabia
Oman
Yemen
Eritrea
Ethiopia
Sudan
Shahneshin
Zagros fold belt
Zagros thrust
Dead Sea trans
Red Sea
Gulf of Aden spreading ridge
Arabian Sea
Ghudun-Khasfah high
East Saharan Craton
Arabian shield
Nubian shield
platform
Sinai
Eastern Desert
Midyan
Ha'il
Hijaz
Asir
Jiddah
Khida
Gabgaba
Gebeit
Halfa
Haya
Bayuda
Takar
Hager
Nafka
Ghedem
30°
40°
60°
50°
20°
10°

Stratigraphic anchors	Height (m)	Age (Ma)	Sedimentation rate
K-Pg Boundary	345,85	66,04	-
Base Maastrichtian	283,8	72,15	1,02
Base hiatus in Razmjooei agemodel	283,8	74,01	0,00
FO *G. aegytiaca*	274	74,42	2,39
LO *M. furcatus*	113	81,00	2,45
LO *D. asymetrica*/Base Campanian	94	84,20	0,59
Kingsdown event/Base Santonian	40	86,49	2,36
Base section with constant sedimentation rate	0	88,19	2,36

FO = First Occurrence; LO = Last Occurrence

Sample ID	Depth (m)	Age (Ma)	La (ppm)	Ce (ppm)	Pr (ppm)	Nd (ppm)	Sm (ppm)	Eu (ppm)	Gd (ppm)	Tb (ppm)	Dy (ppm)	Ho (ppm)	Er (ppm)	Tm* (ppm)	Yb (ppm)	Lu (ppm)	$^{147}Sm/^{144}Nd$	$^{143}Nd/^{144}Nd$	2s	εNd(t)	2s
Insoluble fractions (n=17)																					
ShG E18	333.0	67.31	17.5	27.1	2.85	9.77	1.67	0.333	1.54	0.291	2.3	0.586	2.12	0.33	2.51	0.38	0.103	0.512128	0.000006	-9.01	0.15
ShG E17	311.0	69.47	11.8	19.1	2.07	7.24	1.32	0.254	1.2	0.228	1.77	0.429	1.53	0.24	1.83	0.28	0.110	0.512200	0.000008	-7.63	0.19
ShG E16	292.5	71.29	14.1	20.6	2.11	6.98	1.12	0.234	1.04	0.186	1.44	0.369	1.37	0.21	1.61	0.25	0.097	0.512145	0.000005	-8.56	0.13
ShG E15	271.0	74.54	12	17.7	1.81	6.26	1.12	0.210	1.05	0.188	1.52	0.392	1.43	0.23	1.77	0.26	0.108	0.512217	0.000011	-7.22	0.25
ShG E13	232.0	76.14	16.6	23.8	2.46	8.13	1.46	0.292	1.17	0.223	1.66	0.411	1.47	0.23	1.77	0.27	0.109	0.512254	0.000009	-6.49	0.21
ShG E12	211.7	76.97	16.4	21.3	2.11	6.71	1.05	0.198	0.89	0.161	1.23	0.318	1.15	0.18	1.39	0.22	0.094	0.512222	0.000005	-6.95	0.14
ShG E11	192.0	77.77	17.6	25	2.53	8.29	1.53	0.276	1.25	0.239	1.74	0.425	1.5	0.24	1.85	0.29	0.112	0.512268	0.000008	-6.23	0.20
ShG E10	171.1	78.63	17	24.8	2.57	8.6	1.54	0.318	1.34	0.241	1.76	0.418	1.46	0.23	1.68	0.26	0.108	0.512250	0.000011	-6.53	0.25
ShG E09	152.0	79.41	15.2	21.5	2.26	7.69	1.3	0.234	1.04	0.186	1.45	0.368	1.25	0.19	1.46	0.24	0.103	0.512192	0.000013	-7.60	0.29
ShG E08	132.9	80.19	20.6	27	2.79	9.19	1.46	0.287	1.18	0.210	1.61	0.406	1.42	0.23	1.72	0.27	0.096	0.512174	0.000006	-7.87	0.17
ShG E07	113.0	81.00	19.5	26.2	3.02	10.73	1.99	0.456	1.97	0.325	2.33	0.554	1.84	0.27	1.99	0.31	0.112	0.512237	0.000008	-6.80	0.20
ShG E06	91.8	84.29	8.9	12.3	1.21	3.96	0.71	0.157	0.73	0.157	1.29	0.332	1.15	0.17	1.23	0.19	0.108	0.512167	0.000006	-8.09	0.16
ShG E05	74.2	85.04	17.4	22.2	2.23	7.2	1.19	0.228	1.01	0.177	1.34	0.327	1.17	0.18	1.38	0.22	0.100	0.512245	0.000006	-6.47	0.17
ShG E04	60.0	85.64	13.6	18	1.81	5.96	1	0.208	0.85	0.146	1.06	0.261	0.91	0.14	1.08	0.17	0.102	0.512273	0.000006	-5.95	0.16
ShG E03	39.8	86.50	21.5	29.9	3.21	11.01	2.02	0.418	1.77	0.297	2.16	0.501	1.74	0.27	2.03	0.32	0.111	0.512267	0.000014	-6.14	0.32
ShG E02	22.0	87.26	22.8	29.1	3.04	9.95	1.57	0.309	1.25	0.194	1.38	0.332	1.17	0.18	1.36	0.21	0.095	0.512185	0.000006	-7.56	0.16
ShG E01	1.0	88.15	24.8	31.8	3.46	11.62	1.96	0.402	1.61	0.253	1.73	0.401	1.33	0.21	1.54	0.24	0.102	0.512251	0.000004	-6.34	0.13
														2s external reproducibility:			**± 0.004**		**± 0.000016**		**± 0.35**
Acetic acid leachate (n=18)																					
ShG E18	333.0	67.31	5.1	7.2	1.02	3.89	0.75	0.188	0.78	0.116	0.71	0.149	0.42	0.057	0.38	0.059	0.117	0.512361	0.000007	-4.57	0.17
ShG E17	311.0	69.47	4.9	6.5	0.89	3.45	0.70	0.182	0.76	0.114	0.70	0.150	0.43	0.060	0.41	0.064	0.122	0.512365	0.000006	-4.52	0.14
ShG E16	292.5	71.29	3.6	4.9	0.68	2.68	0.54	0.132	0.58	0.087	0.56	0.118	0.35	0.048	0.32	0.048	0.122	0.512408	0.000008	-3.66	0.19
ShG E15	271.0	74.54	4.8	6.3	0.86	3.41	0.69	0.174	0.78	0.116	0.75	0.163	0.49	0.067	0.45	0.070	0.122	0.512420	0.000007	-3.39	0.17
ShG E14	252.2	75.31	5	5.6	0.90	3.59	0.74	0.185	0.82	0.127	0.85	0.187	0.56	0.077	0.52	0.082	0.124	0.512385	0.000005	-4.10	0.14
ShG E13	232.0	76.14	4.1	6.6	0.87	3.41	0.68	0.162	0.68	0.104	0.65	0.138	0.41	0.056	0.37	0.056	0.120	0.512419	0.000007	-3.38	0.18
ShG E12	211.7	76.97	6.1	7.8	1.02	3.82	0.73	0.180	0.83	0.126	0.82	0.185	0.56	0.079	0.54	0.084	0.115	0.512371	0.000007	-4.25	0.17
ShG E11	192.0	77.77	4.9	8	1.06	4.12	0.80	0.192	0.79	0.119	0.75	0.159	0.46	0.064	0.43	0.066	0.118	0.512403	0.000007	-3.65	0.18
ShG E10	171.1	78.63	5.8	8.5	1.12	4.42	0.90	0.222	0.97	0.142	0.87	0.189	0.56	0.077	0.52	0.080	0.123	0.512374	0.000006	-4.26	0.16
ShG E09	152.0	79.41	4.2	4.6	0.70	2.73	0.53	0.126	0.60	0.088	0.58	0.129	0.40	0.053	0.35	0.052	0.117	0.512355	0.000006	-4.57	0.16
ShG E08	132.9	80.19	4.8	4.9	0.78	3.07	0.59	0.148	0.70	0.104	0.69	0.157	0.47	0.064	0.43	0.067	0.117	0.512348	0.000005	-4.70	0.15
ShG E07	113.0	81.00	7.8	7.8	1.19	4.75	0.91	0.227	1.10	0.158	1.02	0.231	0.69	0.094	0.62	0.098	0.115	0.512339	0.000005	-4.85	0.14
ShG E06	91.8	84.29	7.2	5.7	0.96	4.61	0.96	0.292	1.44	0.171	1.14	0.269	0.84	0.108	0.68	0.117	0.125	0.512325	0.000012	-5.19	0.28
ShG E05	74.2	85.04	9.9	14.3	1.79	6.94	1.34	0.347	1.44	0.214	1.34	0.290	0.87	0.120	0.81	0.125	0.117	0.512394	0.000005	-3.74	0.13
ShG E04	60.0	85.64	8.7	13.8	1.71	6.66	1.28	0.314	1.30	0.193	1.17	0.246	0.71	0.096	0.64	0.098	0.116	0.512403	0.000005	-3.56	0.14
ShG E03	39.8	86.50	7.1	7.3	1.14	5.51	1.16	0.371	1.70	0.208	1.26	0.304	0.91	0.119	0.75	0.111	0.128	0.512377	0.000016	-4.19	0.36
ShG E02	22.0	87.26	5.1	6.9	1.01	4.01	0.78	0.191	0.87	0.128	0.79	0.172	0.50	0.065	0.42	0.064	0.118	0.512345	0.000005	-4.70	0.14
ShG E01	1.0	88.15	6.1	8.1	1.21	4.82	0.95	0.233	0.99	0.148	0.92	0.197	0.58	0.079	0.52	0.080	0.119	0.512365	0.000006	-4.31	0.16
														2s external reproducibility:			**± 0.004**		**± 0.000009**		**± 0.21**
REE concentrations in Certified reference material																					
USGS BHVO-2	Average (n=10)		14.8	36.2	5.15	23.59	5.88	2.000	6.07	0.905	5.23	0.970	2.53	0.320	2.009	0.278	0.1508				
reference values (Jochum et al., 2016):			***15.2***	***37.53***	***5.339***	***24.27***	***6.023***	***2.043***	***6.207***	***0.939***	***5.28***	***0.989***	***2.51***	***0.335***	***1.994***	***0.275***	***0.1501***				
	RSD (%)		*-2.7*	*-3.6*	*-3.6*	*-2.8*	*-2.4*	*-2.1*	*-2.1*	*-3.6*	*-0.9*	*-1.9*	*0.6*	*-3.3*	*0.8*	*0.8*	*0.5*				
USGS BCR-2	Average (n=7)		25.4	53.4	6.81	28.5	6.54	1.945	6.81	1.049	6.48	1.32	3.74	0.520	3.50	0.520	0.139				
reference values (Jochum et al., 2016):			***25.08***	***53.12***	***6.827***	***28.26***	***6.547***	***1.989***	***6.811***	***1.077***	***6.424***	***1.313***	***3.67***	***0.534***	***3.392***	***0.505***	***0.138***				
	RSD (%)		*1.4*	*0.6*	*-0.2*	*0.9*	*-0.1*	*-2.2*	*0.0*	*-2.6*	*0.9*	*0.5*	*1.9*	*-3.2*	*3.2*	*3.0*	*-1.0*				

Reproducibility of the Isotopic measurements of the UGSS BHVO-2 certified reference material

reference value (MC-ICP-MS, Weis al., 2006):	**0.512990**	**0.000010**
average value during the insoluble fraction measurements (JNdi-1 bracketing, n=5):	0.512987	0.000005
average value during the acetic leachate measurements (Rennes-in-house Nd standard bracketing, n=12):	0.512988	0.000007

Sample ID	SiO_2 (%)	Al_2O_3 (%)	Fe_2O_3 (%)	MnO (%)	MgO (%)	CaO (%)	Na_2O (%)	K_2O (%)	TiO_2 (%)	P_2O_5 (%)	Ni (ppm)	Cr (ppm)
G3	9.43	4.72	1.56	< D.L.	0.39	44.57	0.04	0.60	0.18	< D.L.	33.2	63.4
G10	15.39	6.95	2.44	< D.L.	0.51	38.77	0.05	1.02	0.31	< D.L.	33.6	76.6
G22	10.80	3.63	1.42	< D.L.	0.44	44.62	0.05	0.82	0.17	0.12	31.3	45.6
G23	12.21	4.39	1.65	< D.L.	0.46	43.14	0.03	0.94	0.20	0.12	29.9	45.9
G25	13.84	5.15	2.10	0.037	0.49	41.22	0.04	1.09	0.23	0.11	65.6	47.5
G26	13.65	5.06	1.68	< D.L.	0.47	41.73	0.04	1.08	0.23	0.13	22.9	42.4
G32	18.36	6.65	2.26	0.016	0.58	36.61	0.07	1.58	0.31	0.11	46.9	53.4
G38	15.00	4.92	1.76	< D.L.	0.57	40.84	0.06	1.44	0.23	0.12	22.6	40.3
G48	15.25	3.86	1.52	< D.L.	0.57	41.53	0.08	1.14	0.17	0.10	29.2	42.4
G51	12.57	3.18	1.31	< D.L.	0.45	44.02	0.06	0.90	0.14	< D.L.	22.6	33.6
G55	16.27	4.91	1.86	< D.L.	0.64	39.89	0.04	1.17	0.23	< D.L.	32.3	49.7
G60	12.45	4.03	1.52	< D.L.	0.53	43.48	0.03	0.82	0.19	< D.L.	21.1	48.0
G73	10.08	3.32	1.38	< D.L.	0.41	45.88	0.03	0.51	0.15	< D.L.	26.4	47.6
G74	11.23	4.17	1.59	< D.L.	0.44	44.31	0.04	0.55	0.19	< D.L.	32.5	56.9
G82	11.88	4.32	1.70	< D.L.	0.43	43.65	0.05	0.55	0.20	0.10	29.8	58.4
G83	10.99	3.81	1.68	< D.L.	0.45	44.52	0.05	0.51	0.18	0.11	29.0	61.5
G88	11.70	4.52	1.62	< D.L.	0.44	43.81	0.03	0.54	0.21	< D.L.	37.3	66.1
G94	11.44	3.87	1.66	< D.L.	0.54	44.03	0.10	0.61	0.18	0.19	40.8	101
G96	11.30	3.47	1.59	< D.L.	0.54	44.30	0.07	0.60	0.17	< D.L.	48.5	89.8
G102	8.73	2.14	1.14	0.018	0.51	47.89	0.11	0.43	0.11	< D.L.	41.3	53.3
G108	7.63	1.99	1.06	< D.L.	0.52	48.27	0.07	0.40	0.10	< D.L.	40.0	65.7
G120	12.41	3.24	2.29	0.025	1.06	43.59	0.10	0.69	0.18	0.11	83.4	98.5

D.L. : detection limit